

## Modifying transformation pathways in High Entropy Alloys or Complex Concentrated Alloys via thermo-mechanical processing

Bharat Gwalani<sup>a,b</sup>, Stephane Gorsse<sup>c,d</sup>, Deep Choudhuri<sup>a,b</sup>, Mark Styles<sup>e</sup>, Yufeng Zheng<sup>f</sup>, Rajiv S. Mishra<sup>a,b</sup> and R. Banerjee<sup>a, b\*</sup>

<sup>a</sup> Advanced Materials and Manufacturing Processes Institute, University of North Texas  
Denton, TX-76207, USA

<sup>b</sup> Department of Materials Science and Engineering, University of North Texas  
Denton, TX-76207, USA

<sup>c</sup> CNRS, ICMCB, UMR 5026, 33600 Pessac, France  
<sup>d</sup> Bordeaux INP, ENSCBP, 33600 Pessac, France

<sup>e</sup>CSIRO Manufacturing, Private Bag 10, Clayton South, Clayton, 3169, Victoria, Australia

<sup>f</sup>Department of Materials Science and Engineering, The Ohio State University, Columbus, OH  
4310, USA

\*Corresponding Author: Raj.Banerjee@unt.edu

### Abstract

Often the experimentally-observed, single-phase high entropy alloy (HEA) is the result of second-phase precipitation constrained by thermodynamic and kinetic factors. Using  $\text{Al}_{0.3}\text{CoCrFeNi}$  as a candidate HEA, this paper demonstrates the strong influence of thermo-mechanical processing on the transformation pathway adopted for isothermal second-phase precipitation. A traditional thermo-mechanical processing route comprised of homogenization cold-rolling solution treatment in the single *fcc* phase region, followed by a precipitation anneal at a lower temperature, results in a homogeneous distribution of nanometer scale-ordered  $\text{L1}_2$  (gamma prime-like) precipitates within the *fcc* matrix. In contrast, if cold-rolling is followed directly by annealing at the precipitation temperature, then the resulting microstructural evolution pathway changes completely, with concurrent recrystallization of the matrix *fcc* grains and precipitation of  $\text{B2}$  and sigma phases, largely at the grain boundaries. These experimentally observed variations in transformation pathway have been rationalized via the competition between the thermodynamic driving force and activation barrier for second-phase nucleation in this alloy, coupled with the kinetics of the process. The microstructural variations that result from these dramatically different phase transformation pathways can lead to some rather exceptional mechanical properties that can be varied over a large range even for a single  $\text{Al}_{0.3}\text{CoCrFeNi}$  HEA composition.

### Introduction

High Entropy Alloys (HEAs) are an intriguing new class of metallic materials that offer a versatile range of permutations of composition and phase structures with a wide range of structure-property combinations [1-10]. This new class of alloys derives their properties from

being multi-element systems, and can crystallize as simple phase structures despite high concentrations of five or more elements [2-10].

Researcher fascination with HEAs is concentrated on their many superior mechanical and physical properties, some of which are more attractive than commercially-optimized and -used alloys. For example, ultrahigh fracture toughness of some *fcc*-based HEAs is comparable to cryogenic steel [11,12,13], significant resistance to fatigue [9,14], oxidation [15,16] and corrosion in various environments [17-21]; extremely good irradiation resistance [22,23,24]; large strain hardenability [25,26,27]; superconductivity [28]; magnetic properties [29,30,31,32]; high-temperature strength and toughness [33,34,35,36]; and chemical properties [37]. The literature often debates whether the superior properties of HEAs are direct consequences of four core effects; i.e., high entropy, sluggish diffusion, severe lattice distortion and cocktail effect [38, 39, 40]. Due to competition between enthalpy and entropy, these systems should be dealt individually and generalizing any one rule on all these alloys might not be possible or scientifically correct all the time.

Instead, in general, the rich compositional variability of HEAs means they offer tremendous opportunities to micro-engineer the microstructure and manipulate the resultant properties. Several different mechanisms governing the final properties can be activated at the same time in these alloys to attain a cumulative effect on the resultant property. The major concern for *fcc*-based alloys is the lower strength as compared to bcc-based materials. Also, many researchers have critically assessed *fcc* HEAs being similar to multi-component austenitic stainless steels or Ni-based super-alloys, which are often composed of more than two major alloy elements; for example, commercial alloys INCONEL 800 ( $\text{Cr}_{23}\text{Fe}_{46}\text{Ni}_{31}$ ), INCONEL 600 ( $\text{Ni}_{74}\text{Cr}_{18}\text{Fe}_8$ ), and SS 316 ( $\text{Cr}_{18}\text{Fe}_{67}\text{Mn}_2\text{Mo}_1\text{Ni}_{12}$ ). Most of the reported mechanical strength data on *fcc* HEAs suggest strength very similar to that of commercially-used austenitic stainless steels (yield strength = 250-500 MPa and elongation to failure = 5-30%) [6, 8-10, 12, 25, 26, 38-42]. Ni-based alloys provide even higher strength and stability in a wider range of temperatures extending to 900-1000°C [43]. Some precipitation-strengthened stainless steels like PH-17-4 or PH 13-8 offer exceptional room temperature ultimate tensile strength (UTS) of >1.4 GPa. PH steels have an austenitic matrix under solutionized condition (UTS = <700 MPa), but are used mostly after a thermal treatment that induces martensitic transformation along with fine-scale precipitation, which improves strength tremendously. Also, commercial alloys represent exhaustive research and experience to satisfy an exquisite balance of requirements that go far beyond first- and second-tier properties. The minor additions of interstitial elements, focused heat treatment cycles and standardized manufacturing routes have been established to fine-tune the properties that match the requirements for all commercial alloys.

HEAs offer tremendous potential, and identifying the right candidate for coherent applications is important for further development of the alloy. Precipitates and refined grain structure both add to improving material strength. *Fcc*-based  $\text{Al}_{0.3}\text{CoCrFeNi}$  (a quinary HEA) has successfully demonstrated the potential to be precipitation-strengthened via ordered phases [12, 27, 44-47]; it also showed a strong capability for grain boundary strengthening [47]. The addition of Ti, Mo, Nb in  $\text{CoCrFeNi}$  (quaternary alloy) and  $\text{Al}_{0.3}\text{CoCrFeNi}$  alloy systems has further strengthened the alloy at room temperature by forming strong precipitate phases [48-55]. The  $\text{Al}_{0.3}\text{CoCrFeNi}$  alloy displayed high yield strength of 1600MPa in fiber form at 77K [12] and shows good radiation resistance up to 60 peak dpa [23]. The alloy exhibits remarkable resistance to shear

localization and is a potential candidate for penetration protection applications such as armors [56, 57]. Room-temperature strength of the alloy reported so far has been rather low (~300MPa) [27, 58], whereas corrosion resistance was reported to be better than SS 304 and SS 316 [19]. The unique combination of various elements like Al for precipitation strengthening, Cr for corrosion resistance, Ni for strength and creep resistance, and Co for superior creep resistance makes this alloy a perfect candidate for applications such as structural material in pressure water reactors, and in nuclear powers plants if material strength could be improved.

In the current work we used different processing routes to examine the possible phases in an *fcc*-based HEA ( $\text{Al}_{0.3}\text{CoCrFeNi}$ ). The processing history not only influenced the precipitation sequence, precipitate type, size scale and distribution but also provided a range of strength-ductility combinations in the same composition. This work compares strengthening by incoherent/semi-coherent phase precipitation with strengthening by coherent precipitates using the same composition. Varying the inherent strain in the system in the form of defects, dislocations and deformation bands can change the precipitation sequence and result in drastic engineering of the microstructure.

## Experimental Methods

**Materials processing.** HEA of composition  $\text{Al}_{0.3}\text{CoCrFeNi}$  was obtained from Sophisticated Alloys Inc. The as-received alloy was homogenized at  $1150^\circ\text{C}$  for 10 hours. Previous microstructural assessment of the alloy confirmed that the alloy has a single-phase *fcc* crystal structure above  $\sim 1100^\circ\text{C}$  [47]. The homogenized alloy was cold-rolled at room temperature for 90% reduction in thickness and subsequently cut into several slabs. Two different processing routes were followed to process the alloy further (Figure 1). The first route consisted of solutionizing the alloy at high temperature ( $1150^\circ\text{C}$  for 2 mins) to recrystallize the alloy, followed by annealing at a lower temperature of  $620^\circ\text{C}$  for 50 h. It has been previously established that this alloy composition can be precipitation-strengthened by coherent  $\text{L}_1_2$  (ordered *fcc* intermetallic) [47]. The second route aimed at achieving concurrent recrystallization and precipitation at low temperature. Hence the separate recrystallization step at  $1150^\circ\text{C}$  was not done; instead, the cold-rolled slab was aged directly at  $620^\circ\text{C}$  for 50 h. The microstructural details from heat treatments are discussed in the following sections.

**Microstructural characterization.** To analyze the microstructure of the material after processing, pieces were cut and metallographically polished in stages. Final mirror surface finish was achieved by  $0.02 \mu\text{m}$  colloidal silica gel VibroMet<sup>TM</sup> polishing. The crystal orientations and elemental composition were characterized by electron backscattered diffraction (EBSD) and energy dispersive spectroscopy (EDX), respectively, in a FEI Nova Nano scanning electron microscope (SEM). Lift-out samples for Transmission electron microscopy (TEM) and atom probe tomography (APT) were prepared using an FEI Nova 200 dual beam focused ion beam (FIB). TEM analysis was conducted using an FEI Tecnai F20 operated at 200 kV fitted with a STEM-EDS detector. APT experiments were conducted on a CAMECA local electrode atom probe 3000X HR instrument. All experiments were performed in the temperature range of 40–50 K with target evaporation of 0.5% and pulse fraction of 20% of a steady-state applied DC

voltage. APT data reconstruction and analysis were carried out using CAMECA IVAS® 3.6.10 software.

**Synchrotron X-ray Diffraction.** Samples for *in situ* synchrotron studies were prepared with dimensions of 5 mm × 5 mm × 0.5 mm (thickness). The experiment was carried out at the 11-IDC beam-line (111 keV, 1 ¼ 0.117418 Å) of the Advanced Photon Source (APS) at Argonne National Laboratory (ANL). A CeO<sub>2</sub> standard (NIST diffraction intensity standard set: 674a) was used to calibrate the distance between and among the samples and the 2D detector, the position of the beam center and the detector tilt angle. The high energy of the synchrotron beam at APS permitted carrying out the XRD experiments in the transmission mode through relatively thick samples, and led to averaging over substantial sample volumes. The samples were rocked from ±5°, with a square beam of 500 × 500 μm<sup>2</sup> and sample thickness ~ 1000 μm. With an average grain size of ~20 μm,  $\{(500 \times 500 \times 1000) / (20)^3\} \sim 31000$  grains were included in the study. The scattered radiation was collected on a Perkin Elmer 2D detector system. Fit-2D software was used to radially integrate the 2D diffraction data to produce 1D intensity vs. two-theta ( $2\theta$ ) plots. The resulting 1D diffraction data were analyzed using the Pawley method [59], as embodied in TOPAS software (Bruker), to obtain accurate measurements of the lattice parameters for the two phases as a function of temperature.

**Mechanical characterization.** Dog-bone-shaped tensile specimens with gauge length 3 mm were machined from the rolled and annealed sheets by Electrical Discharge Machining (EDM). Both sides of the specimen were ground using SiC paper to achieve final thickness of ~0.7 mm and gauge width of ~ 1.0 mm. Tensile tests were performed at an engineering strain rate of 10<sup>-3</sup> s<sup>-1</sup>. Each test was performed at least three times to ensure consistency; representative results are reported herein. These quasi-static tests used a LVDT (Linear Variable Displacement Transformer) extensometer to perform at least four independent tests to obtain tensile elongation and strength data. The elongation of the gauge length of each sample was measured after testing, and engineering stress–strain curves were calculated from the load-displacement data. Yield strength, ultimate tensile strength, and elongation to failure were determined from the uniaxial tensile stress–strain curves.

**Nomenclature.** The four conditions discussed in detail in this report are 90% cold rolled (**CR**), 90% cold rolled + Solutionized at 1150°C/2mins (**CRSA**), 90% cold rolled + Solutionized at 1150°C/2mins + annealed at 620°C/50h (**CRSA-620**) and 90% cold rolled + directly annealed at 620°C/50h (**CR-620**).

## Results

### *Precipitation in fully-recrystallized fcc microstructure*

#### *a. Cold-rolled microstructure*

The first step in homogenizing the cast Al<sub>0.3</sub>CoCrFeNi alloy was annealing at 1150°C for 10 hrs. The alloy was then cold-rolled (CR) to 90% reduction in thickness. The SEM micrograph and orientation map from the CR condition presented in Figure 2 include a low magnification back scattered electron diffraction (BSED) image (Figure 2 (a)) that shows the severely strained and elongated *fcc* grains after cold rolling. The inverse pole figure (IPF) map from a representative

region, highlighted in the BSED image using a white box in Figure 2 (a)), is Figure 2 (b). This region is located within a single prior *fcc* grain of the parent solution-treated microstructure, and exhibits a high degree of local misorientation, presumably resulting from high dislocation density and the rearrangement of these dislocations into cells and sub-cells as well as the formation of deformation twins (Figure 2 (c)). Furthermore, the black arrows in Figure 2 (b) mark regions at these deformation twin / dislocation cell boundaries, with clear evidence of newly recrystallized fine-scale *fcc* grains forming within the strained prior larger-scale *fcc* matrix grains. Formation of these recrystallized regions within the strained *fcc* matrix grains indicates that severe cold-rolling to 90% not only results in a high density of dislocations, but also that local adiabatic heating in some regions results in initiation of recrystallization. Additionally, deformation twins are also seen in the 90% cold-rolled microstructure, an example of which is shown in Figure 2 (c). A misorientation profile along the vector shown by a yellow arrow in Figure 2 (c) is shown as the inset. Misorientation profiling along the highlighted lines confirmed the bands in the IPF map to be twin fault planes with their characteristic 60° misorientation.

TEM is performed on the 90% cold rolled (CR) condition and the results are shown in Figure 2 (d). Figure 2 (d) shows a low magnification bright field (BF) TEM image. SADPs from [001] and [112̄] zone axes are shown as insets in left bottom and right top respectively. The absence of super lattice spots, or any other additional spots, indicates that no ordering/ precipitation of second phase(s) occurs as a result of cold rolling. A high magnification view of the region marked by the white dotted box in Figure 2 (d) is shown in Figure 2 (e). Deformation bands are clearly observed in this microstructure, arranged in a somewhat periodic manner, and the boundaries of these bands have been previously considered to be geometrically necessary boundaries (GNBs) [60], aligning parallel to the rolling direction (see Figures 2 (c) and (d)). Additionally, fine scale deformation twinning is observed within these macroscopic deformation bands. A selected area diffraction pattern (SADP), recorded from a [011]<sub>fcc</sub> zone axis, is shown as an inset to the figure, where the twin plane is marked by yellow dotted line. The primary reflections of the *fcc*-matrix/twin are related by a mirror symmetry about the dotted straight line joining the higher and lower order (1̄11) reflections. The nano-twins in the lamellar microstructures suggests the transition from dislocation slip dominated, to a twinning-dominated deformation mechanism especially in heavily cold rolling.

Regardless, the severe cold work resulted in a substantially high degree of stored strain energy in the *fcc* matrix, eventually leading to recrystallization, accompanied by the formation of fine-scale new grains in the microstructure during isothermal annealing at 1150°C, as discussed in the subsequent section.

#### *b. Recrystallization at high temperature in single fcc phase region*

A second annealing treatment at 1150°C for 2 mins after cold-rolling resulted in complete recrystallization of the microstructure. The microstructural characterization results from cold-rolled plus solution annealed (CRSA) condition are shown in Figure 3. BSED SEM image from this condition presents an abundance of annealing twins that depict a strain-free and relaxed structure with grain size of ~20 μm (Figure 3 (a)). Furthermore, transmission electron

microscopy (TEM) results confirm that selected area diffraction pattern (SADP) from  $[011]_{fcc}$  zone axis clearly established a single-phase *fcc* structure (Figure 3 (b)).

The atom probe reconstruction from the intra-granular region is shown in Figure 3 (c). All ions appear in the reconstruction, and no partitioning of the element is evident. Hence, the CRSA condition consists of single-phase *fcc* structure with no fine-scale decomposition or second-phase precipitation.

*c. Phase separation followed by ordering transformation (precipitation of ordered L1<sub>2</sub> second phase) on low-temperature aging*

Figures 4, 5, and 6 show TEM results from the CRSA-620 condition, after isothermal annealing of the fully recrystallized sample at 620°C for 50 hrs. Two types of  $[001]_{fcc}$  zone axis SADP patterns, shown in Figures 4(a) and (b), were recorded from this sample, from two different regions. While the majority of regions exhibited the pattern shown in Figure 4(a), a smaller fraction of regions exhibited the pattern shown in Figure 4(b). Figure 4(a) clearly shows extra super-lattice spots at {100} and {110} locations, indicating the possible presence of an L1<sub>2</sub> phase. Additionally, Figure 4(c) shows the  $[011]_{fcc}$  zone axis (ZA) from the same region of the sample, with extra {100} and {110} super-lattice reflections, confirming the presence of the L1<sub>2</sub> phase. A dark-field TEM image recorded from a {001} type superlattice reflection (marked by a circle in Figure 4(a)), clearly reveals these L1<sub>2</sub> precipitates within the *fcc* matrix. Interestingly, the  $[001]_{fcc}$  zone axis SADP shown in Figure 4(b), revealed additional super-lattice reflections, beyond the {100} and {110} type L1<sub>2</sub> reflections. These principal additional super-lattice reflections are located at 1/8{220} locations, as seen in Figure 4(b). Additional SADP patterns, corresponding to the  $[112]_{fcc}$  and the  $[111]_{fcc}$  zone axes are shown in Figures 5(a) and (b) respectively. These diffraction patterns also reveal both super-lattice reflections corresponding to the L1<sub>2</sub> phase, as well as the new ordered phase leading to the 1/8{220} reflections. Further analysis of this new ordered phase has been carried out via preliminary high-resolution TEM investigations, shown in Figure 6. Both high-resolution TEM images, shown in Figures 6(a) and (c), have been recorded along the  $[001]_{fcc}$  viewing direction. An example of an interface between the *fcc* matrix and a L1<sub>2</sub> precipitate is shown in Figure 6(a) with the corresponding fourier transform, shown in Figure 6(b). The L1<sub>2</sub> ordering is clearly visible in this high-resolution TEM image. Figure 6(c) shows a high-resolution TEM image from a precipitate of the second ordered phase with the corresponding fourier transform shown in Figure 6(d). The atomic-resolution image of this ordered phase reveals that the repeat unit cell for this structure consists of eight consecutive {220} *fcc* lattice planes, as marked by the dashed box in Figure 6(c). Such a repeat unit cell will lead to the 1/8{220} reflections observed in the  $[001]_{fcc}$  SADP patterns. The details of the crystal structure, symmetry, and lattice parameters of this new ordered phase in the CRSA-620 condition have not yet been determined, and constitute part of future studies. Nevertheless, the results presented in this paper do establish the presence of a second new ordered precipitate, beyond the L1<sub>2</sub> precipitates. However, the majority precipitates appear to be L1<sub>2</sub> precipitates with only a small fraction of precipitates belonging to the new ordered phase.

Compositional analysis of the precipitates in the CRSA-620 condition has been carried out using energy dispersive spectroscopy (EDS), using a Super EDS detector (Chemi-STEM technique) in an aberration-corrected TITAN TEM. The results as presented in Figure 7 include the following: (a) the HAADF-STEM image from an intra-granular region where the precipitates exhibit a darker contrast; while (b-f) show the compositional maps of the various elements as respectively marked in the figure. The precipitates are rich in Al and Ni and lean in all other elements (Cr, Fe and Co). Based on these Chemi-STEM results from the precipitates, it appears that all samples precipitates have similar compositions. Therefore, it is not possible to distinguish between the L<sub>1</sub><sub>2</sub> precipitates and the precipitates of the new ordered phase, based on this composition analysis. This suggests that the two types of precipitates are quite similar in composition.

Atom probe tomography (APT) results from CRSA-620 condition are shown in Figure 8. Figure 8(a) shows an ionic/atomic APT reconstruction of this sample, together with a section of a dark-field TEM image. The similarity between the size scale and morphology of the precipitates between these two renditions, establishes the fidelity of the atom probe reconstruction. The APT reconstruction in Figure 8(a) shows all the ions/atoms in the sample. Figure 8(b) delineates the precipitates in the APT reconstruction, using a 15% Al iso-concentration surface, together with nickel ions plotted in the same reconstruction. Compositional profiles across the interface between the *fcc* matrix and precipitates (Figure 8(c)) confirm that the precipitates are enriched in Al and Ni, consistent with the Chemi-STEM results. Again, it appears that there is no significant difference between the compositions of these precipitates, captured within the APT reconstruction volume. Therefore, at this point it is not possible to compositionally distinguish the L<sub>1</sub><sub>2</sub> precipitates from the precipitates of the new ordered phase. The compositions of the L<sub>1</sub><sub>2</sub> and *fcc* phase in atomic percent from APT analysis are shown in Table 1.

<b>Fcc phase:</b>	$4.28 \pm 0.03$ Al, $25.62 \pm 0.10$ Co, $27.44 \pm 0.08$ Cr, $14.26 \pm 0.05$ Ni, $28.40 \pm 0.09$ Fe
<b>L<sub>1</sub><sub>2</sub> phase:</b>	$31.81 \pm 0.10$ Al, $6.02 \pm 0.02$ Co, $1.47 \pm 0.02$ Cr, $52.34 \pm 0.13$ Ni, $8.36 \pm 0.03$ Fe

#### *d. In situ investigation of order-disorder reaction via synchrotron XRD*

The high energy of the synchrotron beam at the advanced photon source (APS) permitted carrying out the XRD experiments in the transmission mode through relatively thick samples, and led to averaging over substantial sample volumes. The samples were rocked from  $\pm 5^\circ$ , with a square beam of  $500 \times 500 \mu\text{m}^2$  and sample thickness  $\sim 1000 \mu\text{m}$ . With an average grain size of  $\sim 20 \mu\text{m}$ ,  $((500 \times 500 \times 1000) / (20)^3) \sim 31000$  grains were included in the study. The results of synchrotron diffraction experiments carried out during *in situ* heating and cooling are summarized in the XRD plots in Figure 9. The starting condition for these *in situ* heating-cooling synchrotron experiments was a CRSA-620 sample that contained well-developed L<sub>1</sub><sub>2</sub> precipitates prior to initiation of the heating cycle at the synchrotron.

The rate of heating and cooling was controlled at  $0.5^\circ\text{C}/\text{s}$ . X-ray data were collected throughout the experiment at 18s or  $9^\circ\text{C}$  intervals. The maximum temperature of heating was  $1000^\circ\text{C}$ , where the sample was held for 30 minutes. A few selected plots in Figure 9 show where the fundamental *fcc* ( $\{111\}$  and  $\{200\}$ ) reflections have been plotted in a staggered plot. While heating, the data in the figure were recorded at  $50^\circ\text{C}$  (Black color),  $650^\circ\text{C}$  (Green color), and

900°C (Red color); and while cooling, the data are recorded at 50°C (Blue color). The insets on the left of the figure (the magnified views), clearly reveal the L<sub>1</sub><sub>2</sub> peaks at 50°C and 650°C during heating. The {100} and {110} L<sub>1</sub><sub>2</sub> peaks are labelled in the figures for these two conditions. The L<sub>1</sub><sub>2</sub> peaks do not appear when the temperature rises (inset on left showing the magnified view of XRD trace in red color, recorded at 900°C); and while it cools (inset on right showing the magnified view of XRD trace in blue color, recorded at 50°C). Additionally, an interesting note is the evidence of lattice expansion when comparing initial condition and later condition, where the L<sub>1</sub><sub>2</sub> phase has dissolved. Cahn [61], has examined the lattice parameter changes accompanying order-disorder transformations in several intermetallic phases with a variety of crystal structures. He concluded “the lattice parameter changes are correlated much more closely with the ordering energy than with the mismatch of atomic sizes”. In our system where elements like Ni, Co, Fe and Al have strong tendencies to form unlike bonds accompanied by exothermic energy release, it can be assumed that the ordering energy plays the dominant role in formation of the ordered precipitates. This will result in shorter bond lengths and thus reduce average lattice parameter of the matrix as compared to the fully disordered *fcc* matrix. Such lattice expansion, due to an order-disorder transformation within the matrix, has been reported in Ni-base super alloys [62].

The experimentally measured lattice constant from the major *fcc* diffraction peaks in this case correspond to an average effect of the ordered domains and the surrounding disordered matrix. In the present study, the matrix lattice constants were determined accurately using Rietveld refinement of the synchrotron XRD patterns obtained during *in situ* annealing experiments. Lattice constants were determined from selected data points along the heating and cooling cycles, and are plotted as a function of temperature (Figure 10). At the early stages of the heating cycle, the lattice expanded linearly due to thermal expansion; but above ~670°C, there is a change in the slope with the rate of expansion increasing substantially. The change in the slope or the change in the rate of expansion while heating can be attributed to the order-disorder transition in this alloy, as is clear from Figure 10. This *in situ* heating-cooling cycle, carried out in the synchrotron, resulted in disordering of the ordered alloy; and this disordered random solid solution is retained on cooling to ambient temperature. Furthermore, the lattice parameters of the individual phases: *fcc* and L<sub>1</sub><sub>2</sub> were calculated to be  $3.591 \pm 0.002$  and  $3.596 \pm 0.002$  Å.

#### e. Grain boundary precipitation in fully-recrystallized *fcc* microstructure

Detailed characterization of the grain boundaries of the fully-recrystallized *fcc* grains in the CRSA-620 sample revealed the precipitation of the ordered B<sub>2</sub> phase. Note that the grain boundaries in the CRSA sample (not shown here) did not exhibit any signature of second-phase precipitates [47]. The EBSD results from the grain boundaries in the CRSA-620 sample are shown in Figures 11 (a) and (b). IPF map in Figure 11 (a) is an inverse pole figure (IPF) map of the *fcc* grains where the grain boundary phase is indexed as a bcc-based phase and is highlighted in red color. Pseudo-colored reference stereographic quadrant is shown as inset of Figure 11 (a). The phase map in Figure 11 (b) shows *fcc* phase (matrix) in red color and the bcc-based phase in green color (grain boundary phase). Further detailed investigation of this grain boundary bcc-based phase was carried out via scanning and transmission electron microscopy. Figure 11 (c) is a BSED image from this annealed condition, with a higher magnification image of the

representative grain boundary region chosen for site-specific preparation of a FIB lift-out for TEM study (inset). Figure 11 (d) is a bright-field TEM image of the same grain boundary intermittently decorated with the bcc-based precipitates. The inset in Figure 11 (d) is a micro-diffraction pattern from one of these precipitates; and this pattern can be indexed consistently as the  $\langle 011 \rangle$  zone axis of an ordered bcc based phase, with super-lattice spots at  $\frac{1}{2}\{002\}$  positions, to establish that these precipitates are B2 precipitates. Similar electron diffraction patterns were obtained from other grain boundary B2 precipitates. Figures 11 (e-i) of the STEM-EDS results from this specific grain boundary region confirm that the B2 phase is rich in Al (26.6 at. %) and Ni (45.8 at. %), while being depleted in Co (14.6 at. %), Cr (2.0 at. %), and Fe (10.9 at. %). The composition of the B2 phase is also shown in Table 1.

### ***Concurrent Recrystallization and Precipitation***

The second part of this investigation focused on directly annealing the cold-rolled  $\text{Al}_{0.3}\text{CoCrFeNi}$  alloy, at precipitation temperature 620°C, to evaluate the influence of pre-existing matrix strain and high defect density on recrystallization and second-phase precipitation. The results of microstructural evolution on aging a 90% cold-rolled sample at 620°C for 50 h are shown in Figures 12 and 13. Figure 12 includes EBSD and EDS maps corresponding to phase distribution and compositional partitioning of elements, respectively. The inverse pole figure (IPF) map (Figure 12 (a)) shows fine recrystallized grains with the pseudo-colored reference stereographic quadrant (inset). Phase map demarcating the *fcc*, B2 and sigma regions in the microstructure is displayed in Figure 12 (b). Figure 12 (c-f) are SEM-EDS composition maps corresponding to various elements, where Cr-rich regions correspond to the sigma phase, and Al- and Ni-rich regions are B2, and rest of the microstructure is *fcc* phase. Note that the grain size in this condition ranged from 0.5  $\mu\text{m}$  to 2  $\mu\text{m}$  in contrast to the CRSA-620, where the grain size was ~20  $\mu\text{m}$ . Additionally, XRD results from the CR and CR-620 condition are shown as the supplementary information (see figure S1). The *fcc*, B2 and sigma peaks are marks in the Figure S1. The lattice parameters are calculated for the three phases are: *fcc* -  $a=3.580 \pm 0.002 \text{ \AA}$ , B2 -  $a=2.875 \pm 0.001 \text{ \AA}$  and sigma -  $a=8.79 \pm 0.005 \text{ \AA}$  and  $c=4.55 \pm 0.004 \text{ \AA}$ .

A site-specific FIB lift-out was prepared for further TEM investigation (Figure 13). Figure 13 (a) shows the STEM image displaying the overall microstructure with the different phases appropriately labeled. The [011] zone axis SADP from an *fcc* matrix grain is an inset in Figure 13 (a), while the [011] zone axis SADP from a B2 grain is Figure 13 (b); and Figures 13 (c and d) show SADPs from two different orientations of sigma grains (as labeled in Figure 13 (a)). The absence of superlattice spots in the *fcc* SADP (Figure 13 (a)) clearly establishes that the *fcc* matrix did not undergo any ordering transformation in this condition. The STEM EDS maps of compositional partitioning across the phases are displayed in Figure 13 (e). TEM results are very similar to SEM observations that depict the sigma phase rich in Cr and B2-rich in Ni and Al.

Atom probe tomography results from CR-620 are explained in Figure 14. The two reconstructions in Figure 14 (a) include the one on the left side capturing only the *fcc* matrix; and

the one on the right side capturing a sigma/B2 interface. A proximity histogram of the 3-dimensionally averaged compositional profile across the sigma/B2 interface clearly shows compositional partitioning across these two phases, with enrichment of Ni and Al within B2; and Cr, Co, Fe enrichment within the sigma phase. Compositions of the three phases in atomic percent as obtained from APT analysis are shown in Table 2.

**Fcc phase:**  $6.55 \pm 0.01$  Al,  $23.97 \pm 0.03$  Co,  $19.91 \pm 0.03$  Cr,  $26.30 \pm 0.03$  Ni,  $23.28 \pm 0.03$  Fe,

**B2 phase:**  $34.98 \pm 0.13$  Al,  $10.85 \pm 0.07$  Co,  $1.26 \pm 0.02$  Cr,  $44.65 \pm 0.16$  Ni,  $8.26 \pm 0.06$  Fe,

**Sigma phase:**  $2.54 \pm 0.03$  Al,  $21.58 \pm 0.10$  Co,  $49.69 \pm 0.18$  Cr,  $6.48 \pm 0.05$  Ni,  $19.69 \pm 0.10$  Fe

### ***Effect of microstructure on mechanical properties***

Samples of the three conditions, CRSA, CRSA-620 and CR-620, were tensile-tested, and the corresponding engineering stress-strain plots are shown in Figure 15. The CRSA condition has yield strength (YS)  $\sim 230$  MPa and ultimate tensile strength (UTS)  $\sim 550$  MPa, with an elongation to failure (EF) of  $\sim 60\%$ , accompanied by substantial strain hardening. The CRSA-620 condition with the fcc + L<sub>1</sub><sub>2</sub> microstructure exhibited YS  $\sim 480$  MPa, UTS  $\sim 820$  MPa and EF of  $\sim 45\%$ . The increase in strength due to precipitation of the ordered intermetallic L<sub>1</sub><sub>2</sub> phase can be observed clearly in this case. In the CR-620 condition, which consists of a fine-scale mixture of three phases consisting of fcc grains, B2 and sigma precipitates, YS  $\sim 820$  MPa, UTS  $\sim 1050$  MPa and EF is reduced to  $\sim 35\%$ . Hence, the prior thermo-mechanical treatment not only influenced the microstructural evolution but also had an immense impact on the strength-ductility properties of this alloy.

## **Discussion**

### ***Experimentally observed transformation pathway***

The two thermomechanical processing routes followed to process the Al<sub>0.3</sub>CoCrFeNi alloy resulted in extremely different microstructures. A schematic correlating the processing route to the resultant microstructure is shown in Figure 16.

While the CRSA-620 condition mainly exhibited a microstructure consisting of an fcc matrix, together with intra-granular nanoscale ordered precipitates, and grain boundary B2 precipitates, the CR-620 condition exhibited a three-phase microstructure comprised of a fine ( $1\text{-}3$   $\mu\text{m}$ ) grain size fcc matrix with grains of  $\sigma$  and B2 phases precipitating along the grain boundaries (or sub-grain boundaries) as well as interphase boundaries.

### ***Microstructural evolution in case of the CRSA-620 condition***

The isothermal annealing at 620°C after fully recovering and recrystallizing the 90% cold-rolled sample (via high temperature annealing at 1150°C) resulted in an fcc matrix with a grain size of

$\sim 20 \mu\text{m}$  and ordered precipitates of size scale 20-50 nm. The majority of ordered precipitates were consistently indexed at L<sub>1</sub><sub>2</sub> phase, though a second ordered phase was also observed. The atomic-resolution image of this new ordered phase reveals that the repeat unit cell for this ordered structure consists of eight consecutive {220} fcc lattice planes. The details of the crystal structure, symmetry, and lattice parameters of this new ordered phase forming in the CRSA-620 condition, constitutes part of future study.

### ***Microstructural evolution in case of the CR-620 condition***

Direct annealing of the Al<sub>0.3</sub>CoCrFeNi alloy, at 620°C, after cold rolling to a thickness reduction of 90%, results in a completely different transformation pathway as compared to isothermal annealing at 620°C after fully recovering and recrystallizing the 90% cold-rolled sample (via high temperature annealing at 1150°C). This direct annealed condition, referred to in this paper as the CR-620 condition, the recovery and recrystallization processes occur concurrently (or in close succession) with precipitation of the ordered intermetallic phases. Thus, recrystallization initiates in the cold-rolled microstructure on the deformation bands which are a mixture of deformation twins and regions with a high dislocation density. This recrystallization results in the development of local regions with fully recrystallized fine scale fcc grains. Early stages of such recrystallization can be observed even in case of the as cold-rolled sample (refer to Fig. 1(b)), prior to any annealing. Based on the final microstructure, it can be presumed that concurrently with recrystallization, the grain boundaries in these fine-grained recrystallized regions act as heterogeneous nucleation sites for both the B2 and  $\sigma$  phases, resulting in the development of a fine-grained three-phase fcc + B2 +  $\sigma$  microstructure. With increasing annealing period, this fine-grained three-phase microstructure spreads across the entire sample. The details with regards to specific nucleation sites of the B2 and  $\sigma$  phases, and their evolution, are yet to be investigated and will be the subject of future study.

### ***Thermodynamic modeling of phase stability and transformations***

The isopleth section with varying Al content for the Al<sub>x</sub>CoCrFeNi system (Figure 17 (a)) is calculated using computational thermodynamic (CALPHAD approach) with input from the TCHEA2 thermodynamic assessment from ThermoCalc [63]. The composition Al<sub>0.3</sub>CoCrFeNi, corresponding to the alloy under investigation, is marked with a vertical dotted line on this isopleth, and the temperature of 620°C is marked with a horizontal dotted line. The intersection of these two dotted lines in Figure 17 (a) predicts that the thermodynamic stable phases for this composition at 620°C are fcc + B2 +  $\sigma$ . The ordered L<sub>1</sub><sub>2</sub> phase is not thermodynamically stable at this temperature, as ascertained by the calculated fractions of the equilibrium phase fractions in this alloy as a function of temperature (Figure 17 (b)) based on the predictions afforded by the thermodynamic models. At 620 °C, the predicted molar fractions of the different phases are 40.3 % fcc (disordered), 38.9 % B2 (ordered bcc) and 20.8 % sigma ( $\sigma$ ). Consequently, the homogeneous intra-granular precipitation of L<sub>1</sub><sub>2</sub> ( $\gamma'$ ) precipitates within the fcc matrix in the case of isothermal annealing of a homogenized and fully-recrystallized Al<sub>0.3</sub>CoCrFeNi alloy at 620°C for 50 hrs is rather interesting. By contrast, direct isothermal annealing at 620°C for 50 hrs, after cold-rolling to 90% (without an intermediate recrystallization anneal at 1150°C), resulted in

precipitation of the equilibrium *fcc* + B2 +  $\sigma$  phases, without any L1<sub>2</sub> ( $\gamma'$ ) precipitation. These results clearly indicate the influence of thermo-mechanical processing on the solid-solid phase transformation pathway adopted by this alloy. To understand the differences between both thermal treatments, we considered the kinetics of onset precipitate nucleation, which is the first stage during precipitate formation.

Nucleation is driven by the reduction in chemical super saturation of the matrix, and depends at the beginning on composition and temperature. The Al<sub>0.3</sub>CoCrFeNi *fcc* solid solution is metastable at 620°C (Figures. 17 (a) and (b)); as a consequence, there is a thermodynamic possibility for the formation of new phases. Positive onset driving forces for nucleation of stable B2 &  $\sigma$  and metastable L1<sub>2</sub> & *bcc* phases from the supersaturated *fcc* matrix (Figure 18 (a)), calculated from the description of the Gibbs free energy curves, show the competition between and among different precipitate types. The B2 phase has the maximum driving force among the three different phases at 620°C; while L1<sub>2</sub>,  $\sigma$ , and *bcc* phases have similar driving forces, with L1<sub>2</sub> being marginally higher. While the experimental results from the CR-620 are in agreement with the thermodynamic prediction of *fcc* + B2 +  $\sigma$  phases, the CRSA-620 condition primarily exhibits *fcc* + L1<sub>2</sub> as the major phases, with a small fraction of B2 precipitates at the grain boundaries. The possible effect of nucleation rate of the different phases is discussed briefly to explain this difference between the microstructures of the two conditions.

According to classical nucleation theory [64], the most important parameter controlling nucleation rate is the activation barrier for nucleus formation. For spherical precipitates forming in a perfect lattice with no strain, the nucleation barrier can be expressed as:

$$\Delta G^* = \frac{16}{3} \pi \frac{\gamma^3}{\Delta G_V^2}$$

where  $\gamma$  is the interfacial energy between the precipitating second phase and the *fcc* matrix and  $\Delta G_V$  is the onset driving force for precipitation.

Since the interfacial energy values for the L1<sub>2</sub> or *bcc* or B2 or  $\sigma$  phases precipitating within the *fcc* matrix of this HEA are not available and are rather difficult to compute, as a first approximation, these values have been adopted from other conventional alloy systems. Since computed and experimental values for  $\gamma/\gamma'$  interfacial energy in Ni-Al system range between 8 and 24 mJ/m<sup>2</sup> [65-68], we considered this range for the  $\gamma$  (*fcc*/L1<sub>2</sub>) interfacial energy. Estimates for  $\gamma$  (*fcc*/*bcc*) interfacial energy range between 180 and 660 mJ/m<sup>2</sup> in Fe-Ni and Ni-Cr systems [69-74]; this range of values was selected for the  $\gamma$  (*fcc*/*bcc*) and  $\gamma$  (*fcc*/B2) interfacial energy. The  $\gamma$  (*fcc*/ $\sigma$ ) interfacial energy is supposed to be higher, and we assumed a realistic range of 500-800 mJ/m<sup>2</sup> [75].

Figure 18 (b) shows clearly that the normalized nucleation barrier ( $\Delta G^*/kT$ ) for the L1<sub>2</sub> phase is the minimum, due largely to the low  $\gamma$  (*fcc*/L1<sub>2</sub>) interfacial energy, a consequence of the fact that the ordered L1<sub>2</sub> phase is based on the same parent *fcc* structure or lattice as the matrix *fcc* phase. In contrast, the substantially larger  $\gamma$  (*fcc*/B2) and  $\gamma$  (*fcc*/ $\sigma$ ) interfacial energies led to much higher values of  $\Delta G^*/kT$  for the B2 (based on a parent *bcc* structure) and  $\sigma$  (very large lattice

parameter, tetragonal structure) phases. Both the B2 and  $\sigma$  phases form semi-coherent or incoherent interfaces with the *fcc* matrix and hence have a high nucleation barrier. Therefore, in case of CRSA-620 condition where the matrix consists of fully-recrystallized, strain-free *fcc* grains, the high nucleation barrier for the B2 and  $\sigma$  phases complicates homogeneous nucleation throughout the matrix. The grain boundaries are the only heterogeneous nucleation sites amenable to precipitation of these phases, and the lower value of the nucleation barrier for the B2 phase as compared with the  $\sigma$  phase makes it easier to precipitate the B2 phase at these grain boundaries. Within the fully-recrystallized *fcc* grains in the CRSA-620 condition, the lower  $\Delta G^*$  for the L<sub>1</sub><sub>2</sub> phase leads to a homogeneous nanometer scale precipitation of this phase, despite the fact that, from a thermodynamic perspective, the L<sub>1</sub><sub>2</sub> phase is a metastable phase. These simple thermodynamic considerations suggest that formation of the L<sub>1</sub><sub>2</sub> phase may be favored due to higher homogenous nucleation rate compared to other competing equilibrium phases.

On the contrary, in case of the sample that was directly annealed after cold-rolling at 620°C, (the CR-620 condition), the precipitation of second phases occurs under rather different circumstances. As discussed previously, the 90% cold-rolled microstructure consists of a high density of dislocations and deformation twins, as well as of localized recrystallized regions with fine-scale *fcc* grains. The presence of these defects; i.e., deformation twin boundaries, dislocation cell walls, and grain boundaries between the fine recrystallized grains forming during rolling, all act as heterogeneous nucleation sites for the equilibrium B2 and  $\sigma$  phases within the prior *fcc* matrix, and consequently reduce the heterogeneous nucleation barrier (lower  $\Delta G_{het}^*$ ). Therefore, the sequence of phase evolution in the CR-620 condition involves concurrent recrystallization of fine-scale *fcc* grains and the heterogeneous precipitation of B2 and  $\sigma$  phases. This results in a homogeneous distribution of all three phases — *fcc* + B2 +  $\sigma$  within the microstructure — and leads to an excellent balance of high strength, very good ductility, and excellent strain-hardenability.

### ***Influence of microstructure on tensile properties***

As shown earlier in this paper, the CRSA, CRSA-620, and CR-620 conditions of the *fcc*-based Al<sub>0.3</sub>CoCrFeNi HEA exhibit strikingly different tensile properties. While the CRSA and CRSA-620 samples had relatively coarse *fcc* grains ( $\sim 20 \mu\text{m}$ ), the CR-620 sample had a highly refined recrystallized microstructure with  $\sim 1\text{-}3 \mu\text{m}$  *fcc* grains. Previous work clearly demonstrates that this alloy exhibits a very large Hall-Petch hardening coefficient, and a Hall-Petch type relationship has been determined for the yield strength of the single *fcc* phase in this alloy [47]:

$$\sigma_{HP} = \sigma_0 + K_{HP} d^{-1/2},$$

with the Hall-Petch coefficients,  $K_\sigma$  and intrinsic yield strength of the alloy  $\sigma_0$ , being 824 MPa ( $\mu\text{m}^{0.5}$ ) and 95 MPa respectively [47]. Based on this it can be concluded that the CR-620 sample will exhibit a substantially higher yield strength as compared to the CRSA-620 and CRSA samples in agreement with the experimentally measured tensile properties. While the CRSA-620 sample contains a nanometer-scale distribution of L<sub>1</sub><sub>2</sub> precipitates the total phase fraction of these intermetallic precipitates is only  $\sim 20\%$ , based on approximate measurements using dark-

field TEM images. This L<sub>1</sub><sub>2</sub> phase fraction is quite low considering that present day commercially-used nickel-base superalloys in turbine jet engines typically contain greater than 50% γ' (L<sub>1</sub><sub>2</sub>) precipitates in the *fcc* Ni-base matrix [76]. Therefore, in case of the Al<sub>0.3</sub>CoCrFeNi HEA, there is only a limited degree of precipitation strengthening that can be achieved via L<sub>1</sub><sub>2</sub> precipitates. Consequently, while the CRSA-620 sample exhibits a higher strength as compared to the CRSA sample, its strength is substantially lower than that of the finer grained CR-620 sample. In addition to the finer *fcc* grain size, the intermetallic B2 and σ precipitates present in the CR-620 sample lead to additional strengthening of this sample.

## Summary and Conclusion

The effect of thermo-mechanical treatment on phase evolution in an *fcc*-based Al<sub>0.3</sub>CoCrFeNi HEA was investigated. While the alloy was precipitation strengthenable [47] by introducing hard-coherent intermetallic phase in the matrix via the first processing route, the second route achieved the equilibrium phases. The following can be established from the current study:

1. Strain-free, single-phase *fcc* structure in this alloy when aged at 620°C for 50 h resulted primarily in a *fcc* + L<sub>1</sub><sub>2</sub> microstructure with B2 pinning the grain boundaries. An additional second ordered phase was found in this condition, with a much larger unit cell and a repeat unit of eight {220} *fcc* planes.
2. The order-disorder transition associated with the formation of the L<sub>1</sub><sub>2</sub> phase in this HEA was investigated via *in situ* synchrotron XRD annealing experiments, and the order-disorder transition temperature was determined to be ~670°C.
3. Strained single-phase *fcc* structure when aged at 620°C for 50 h resulted in a tri-phase mixture of *fcc* + B2 + sigma phase.
4. CALPHAD predictions using Thermo-Calc were to justify the results obtained via the second processing route. Thermodynamic calculations illustrate that the precipitation of the L<sub>1</sub><sub>2</sub> phase observed in the first processing route can be explained by homogeneous nucleation, while the possible effect of heterogeneous nucleation of B2 and σ during the second processing route was discussed.
5. Changes in mechanical properties associated with microstructural changes are clear.

The results presented in this paper led to some fundamental insights into the change in transformation pathway depending on the prior condition of the sample. This approach can be used effectively in other HEAs or in general in other alloy systems.

## Acknowledgement

The work was performed under a cooperative agreement between the Army Research Laboratory and the University of North Texas (W911NF-16-2-0189). The authors also acknowledge the DOE's Advanced Proton Source at the Argonne National Lab for providing access and user time on the beam line for x-ray diffraction experiments and would like to acknowledge Dr. Yang Ren for his support and guidance at the APS facility. The authors also acknowledge the Materials

Research Facility (MRF) at the University of North Texas for use of microscopy and atom probe tomography facilities, and the Center for Electron Microscopy and Analysis (CEMAS) at the Ohio State University, for microscopy facilities.

## **Figure Captions:**

**Figure 1.** A schematic showing the two different processing routes adopted for processing the Al<sub>0.3</sub>CoCrFeNi alloy

**Figure 2.** 90 % Cold rolled Al<sub>0.3</sub>CoCrFeNi alloy: (A) BSED image showing the strained microstructure. (B) Inverse Pole Figure (IPF) map from the region marked by a white box in (A) (C) High magnification IPF from the region highlighted by a red colored box shown in (B). Inset of (D) shows the mis-orientation angle profile across the red arrow in the figure (C). (D and E) TEM results from CR 90% condition: (D) shows the BFTEM image with the SADP from [001]<sub>fcc</sub> and [1-1-2]<sub>fcc</sub> shown as the inset on left and right respectively. (E) High magnification image showing the twin faults in the matrix. Inset of the image shows the SADP from [011]<sub>fcc</sub> zone showing mirror symmetry about the yellow dotted lines.

**Figure 3.** Cold rolled (90%) plus Solutionized (1150 °C/ 2 min) Al<sub>0.3</sub>CoCrFeNi alloy (CRSA): (A) BSED image showing the recrystallized grain structure. (B) SADP from [011]<sub>fcc</sub> ZA showing the fundamental *fcc* diffraction spots. (C) APT reconstruction showing a homogeneous distribution of all ions.

**Figure 4.** (CRSA-620): (A and B) SADP from [001]<sub>fcc</sub> ZA from two different regions(C) SADP from [011]<sub>fcc</sub> ZA showing the super-lattice spots corresponding to the ordered L1<sub>2</sub> phase. (D) Dark field image made from the superlattice spot highlighted in (A) showing the lighted-up L1<sub>2</sub> precipitates.

**Figure 5.** (CRSA-620): (A and B) SADP patterns from [1-1-2]<sub>fcc</sub> and [-111]<sub>fcc</sub> respectively, showing the presence of an extra spots corresponding to an additional new phase apart from the ordered L1<sub>2</sub> in the matrix.

**Figure 6.** (CRSA-620): (A) Atomic resolution TEM image showing the *fcc* + L1<sub>2</sub> phase atomic columns and (B) the corresponding FFT image. (C) atomic resolution TEM image from the region consisting of *fcc* + new ordered phase and (D) the corresponding FFT image.

**Figure 7.** (CRSA-620): (A) STEM image (B-F) STEM EDS maps for various elements as labelled.

**Figure 8.** (CRSA-620): (A) DFTEM and APT reconstruction from the inter-granular region showing the alignment of the L1<sub>2</sub> precipitates (B) Al iso-surface (gray color) highlighting the nano precipitates (C) proximity histogram across the interface between the precipitates and *fcc* matrix showing the compositional partitioning.

**Figure 9.** Synchrotron XRD results from CRSA-620 condition while *in situ* heating and cooling of the sample.

**Figure 10.** CRSA-620: *fcc* lattice parameter vs temperature while heating to 1000 °C and cooling to room temperature.

**Figure 11.** CRSA-620 - Grain boundary: (A)OIM: IPF map (B)OIM: phase map (C) BSED image showing the dark contrast grain boundary precipitate (inset shows the higher

magnification BSED image from the grain boundary) (D) STEM image with the SADP as the inset from the grain boundary phase consistently indexed as an ordered bcc (B2) phase. (E-I) compositional maps from the grain boundary region. B2 is rich in Al and Ni.

**Figure 12.** Cold rolled (90%) plus annealed at 620 °C for 50 h (*without high temperature recrystallization*) (CR-620): (A)OIM: IPF map (B)OIM: phase map (C-F) compositional maps clearly showing partitioning in sigma ( $\sigma$ ), B2 and fcc phases.

**Figure 13.** TEM results from CR-620: (A) STEM image, inset (SADP from [011] fcc grain), (B) SADP from [011]<sub>B2</sub> zone axis. (C) and (D) SADP from [011] <sub>$\sigma$</sub>  and [001] <sub>$\sigma$</sub> . (E) STEM EDS maps for Ni(cyan) Al (red), Fe (purple) and Cr (blue) as labeled in the figure.

**Figure 14.** APT from CR-620 (A) reconstructions from two different tips (B) proximity histogram from  $\sigma$ -B2 interface showing the compositional partitioning.

**Figure 15.** Stress-strain curve from three different heat treatment conditions from  $\text{Al}_{0.3}\text{CoCrFeNi}$  alloy.

**Figure 16.** Schematic showing the two different transformation pathways based on heat treatments resulting in starkly different microstructures.

**Figure 17.** (A) Calculated isopleth of the  $\text{Al}_x\text{CoCrFeNi}$  with  $x=0-1$ , (B) calculated molar fraction of equilibrium phases as a function of the temperature for the  $\text{Al}_{0.3}\text{CoCrFeNi}$  alloy composition. The dotted lines show the temperature of 620°C and the composition of  $\text{Al}_{0.3}\text{CoCrFeNi}$ .

**Figure 18.** (A) Onset driving forces and (B) range of normalized nucleation barriers for homogenous precipitation of L1<sub>2</sub>, B2, bcc and  $\sigma$  phases from the supersaturated fcc solid solution with  $\text{Al}_{0.3}\text{CoCrFeNi}$  composition. The dotted line indicates the temperature of 620°C.

**S1:** X-ray diffraction plots from CR and CR620 conditions.

### Tables captions:

**Table 1.** Compositions of the *fcc* matrix, L1<sub>2</sub> and grain boundary (GB) B2 phase in atomic percent from APT and CHEMI-STEM EDS in CRSAs-620 condition.

Characterization Technique	Phase	Al	sigma	Co	sigma	Cr	sigma	Ni	sigma	Fe	sigma
APT	FCC	4.28	0.3	25.62	0.1	27.44	0.8	14.26	0.5	28.4	0.9
APT	L1 <sub>2</sub>	31.81	0.5	6.02	0.2	1.47	0.2	52.34	0.9	8.36	0.3
STEM EDS	GB B2	26.6	1.3	14.6	0.9	2	0.2	45.8	1.6	10.9	0.6

**Table 2.** Compositions of the *fcc* matrix, B2 and Sigma phase in atomic percent from APT and in CR-620 condition.

Phase	Al	sigma	Co	sigma	Cr	sigma	Ni	sigma	Fe	sigma
FCC	6.55	0.1	23.97	0.6	19.91	0.3	26.3	0.3	23.28	0.4
B2	34.98	0.3	10.85	0.3	1.26	0.2	44.65	0.8	8.26	0.2
Sigma	2.54	0.3	21.58	0.4	49.69	0.9	6.48	0.1	19.69	0.3

### References

1. Callister, William D., and David G. Rethwisch. Materials science and engineering: an introduction. Vol. 7. New York: Wiley, 2007.
2. Dowling, Norman E. Mechanical behavior of materials. Pearson, 2012.
3. Yeh, J-W., S-K. Chen, S-J. Lin, J-Y. Gan, T-S. Chin, T-T. Shun, C-H. Tsau, and S-Y. Chang. “Nanostructured high-entropy alloys with multiple principal elements: novel alloy design concepts and outcomes.” Advanced Engineering Materials 6, no. 5 (2004): 299-303.
4. Yeh, Jien Wei, Yu Liang Chen, Su Jien Lin, and Swe Kai Chen. “High-entropy alloys—a new era of exploitation.” In Materials Science Forum, vol. 560, pp. 1-9. Trans Tech Publications, 2007.
5. B. Cantor, I.T.H. Chang, P. Knight, A.J.B. Vincent, Microstructural development in equiatomic multicomponent alloys, Mater. Sci. Eng. A 375-377 (2004) 213-218.
6. Jien-Wei, Y. “Recent progress in high entropy alloys.” Ann. Chim. Sci. Mat 31, no. 6 (2006): 633-648.
7. Sheng, G.U.O., and Chain Tsuan LIU. “Phase stability in high entropy alloys: formation of solid-solution phase or amorphous phase.” Progress in Natural Science: Materials International 21, no. 6 (2011): 433-446.

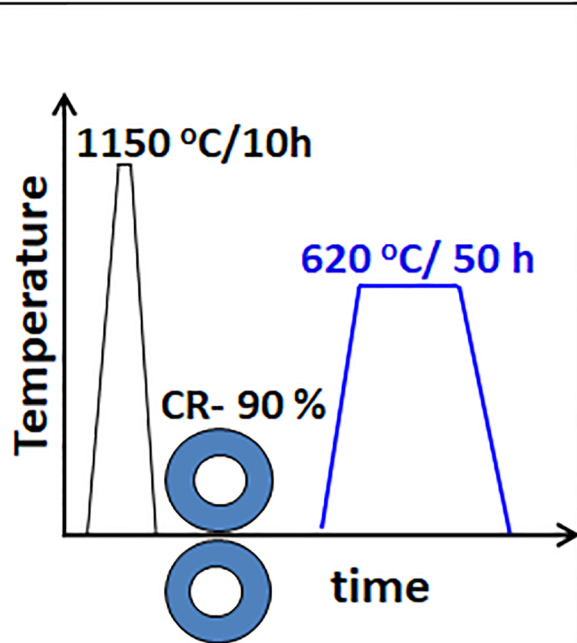
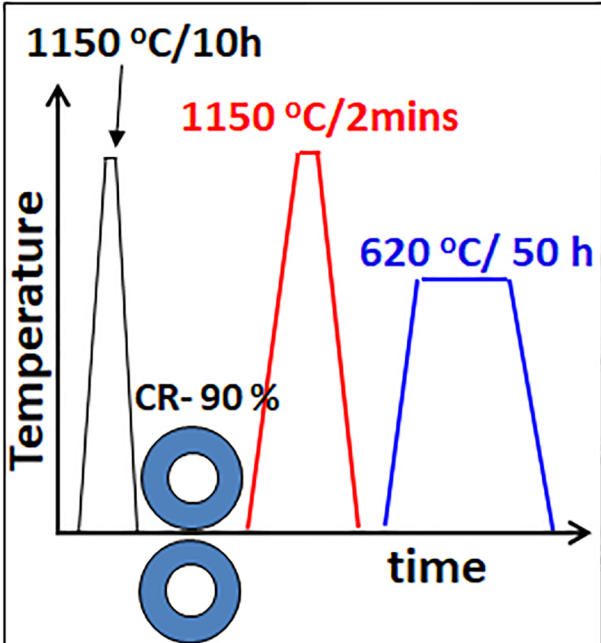
8. Miracle, Daniel B., Jonathan D. Miller, Oleg N. Senkov, Christopher Woodward, Michael D. Uchic, and Jaimie Tiley. "Exploration and development of high entropy alloys for structural applications." *Entropy* 16, no. 1 (2014): 494-525.
9. Zhang, Yong, Ting Ting Zuo, Zhi Tang, Michael C. Gao, Karin A. Dahmen, Peter K. Liaw, and Zhao Ping Lu. "Microstructures and properties of high-entropy alloys." *Progress in Materials Science* 61 (2014): 1-93.
10. Choudhuri, D., B. Gwalani, S. Gorsse, C.V. Mikler, R.V. Ramanujan, M.A. Gibson, and R. Banerjee. "Change in the primary solidification phase from fcc to bcc-based B2 in high entropy or complex concentrated alloys." *Scripta Materialia* 127 (2017): 186-190.
11. Gludovatz, Bernd, Anton Hohenwarter, Keli VS Thurston, Hongbin Bei, Zhenggang Wu, Easo P. George, and Robert O. Ritchie. "Exceptional damage-tolerance of a medium-entropy alloy CrCoNi at cryogenic temperatures." *Nature Communications* 7 (2016).
12. Li, Dongyue, Chengxin Li, Tao Feng, Yidong Zhang, Gang Sha, John J. Lewandowski, Peter K. Liaw, and Yong Zhang. "High-entropy Al<sub>0.3</sub>CoCrFeNi alloy fibers with high tensile strength and ductility at ambient and cryogenic temperatures." *Acta Materialia* 123 (2017): 285-294.
13. Gludovatz, Bernd, Anton Hohenwarter, Dhiraj Catoor, Edwin H. Chang, Easo P. George, and Robert O. Ritchie. "A fracture-resistant high-entropy alloy for cryogenic applications." *Science* 345, no. 6201 (2014): 1153-1158.
14. Hemphill, Michael Alexander, T. Yuan, G.Y. Wang, J.W. Yeh, C.W. Tsai, A. Chuang, and P.K. Liaw. "Fatigue behavior of Al<sub>0.5</sub>CoCrCuFeNi high entropy alloys." *Acta Materialia* 60, no. 16 (2012): 5723-5734.
15. C.M. Liu, H.M. Wang, S.Q. Zhang, H.B. Tang, A.L. Zhang, Microstructure and oxidation behavior of new refractory high entropy alloys, *J. Alloys Compd.* 583 (2014) 162-169.
16. O.N. Senkov, S.V. Senkova, D.M. Dimiduk, C. Woodward, D.B. Miracle, Oxidation behavior of a refractory NbCrMo0.5Ta0.5TiZr alloy, *J. Mater. Sci.* 47 (2012) 6522-6534.
17. Hsu, Yu-Jui, Wen-Chi Chiang, and Jiann-Kuo Wu. "Corrosion behavior of FeCoNiCrCu x high-entropy alloys in 3.5% sodium chloride solution." *Materials Chemistry and Physics* 92, no. 1 (2005): 112-117.
18. Qiu, Xing-Wu, Yun-Peng Zhang, Li He, and Chun-ge Liu. "Microstructure and corrosion resistance of AlCrFeCuCo high entropy alloy." *Journal of Alloys and Compounds* 549 (2013): 195-199.
19. Chen, Y.Y., T. Duval, U.D. Hung, J.W. Yeh, and H.C. Shih. "Microstructure and electrochemical properties of high entropy alloys—a comparison with type-304 stainless steel." *Corrosion Science* 47, no. 9 (2005): 2257-2279.
20. Lee, C.P., Y.Y. Chen, C.Y. Hsu, J.W. Yeh, and H.C. Shih. "Enhancing pitting corrosion resistance of Al<sub>x</sub>CrFe 1.5 MnNi 0.5 high-entropy alloys by anodic treatment in sulfuric acid." *Thin Solid Films* 517, no. 3 (2008): 1301-1305.
21. Lee, C.P., C.C. Chang, Y.Y. Chen, J.W. Yeh, and H.C. Shih. "Effect of the aluminium content of Al<sub>x</sub>CrFe1.5MnNi 0.5 high-entropy alloys on the corrosion behaviour in aqueous environments." *Corrosion Science* 50, no. 7 (2008): 2053-2060.

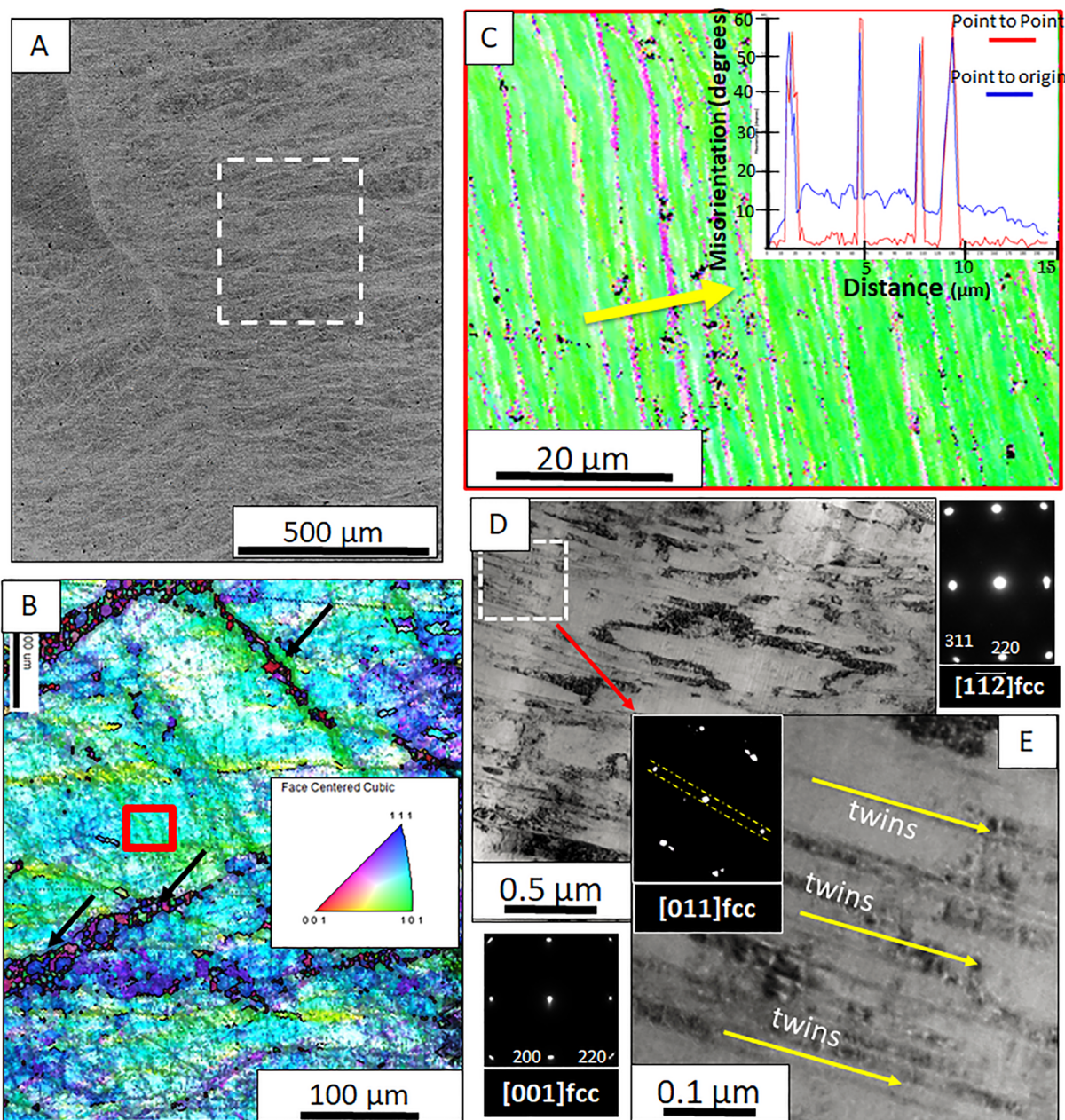
22. Xia, Song-qin, W.A.N.G. Zhen, Teng-fei Yang, and Yong Zhang. "Irradiation behavior in high entropy alloys." *Journal of Iron and Steel Research, International* 22, no. 10 (2015): 879-884.
23. Liaw, Peter K. "Radiation Behavior of High-Entropy Alloys for Advanced Reactors." (2015).
24. Lu, Chenyang, Liangliang Niu, Nanjun Chen, Ke Jin, Taini Yang, Pengyuan Xiu, Yanwen Zhang et al. "Enhancing radiation tolerance by controlling defect mobility and migration pathways in multicomponent single-phase alloys." *Nature Communications* 7 (2016).
25. Otto, Frederik, A. Dlouhý, Ch Somsen, Hongbin Bei, G. Eggeler, and Easo P. George. "The influences of temperature and microstructure on the tensile properties of a CoCrFeMnNi high-entropy alloy." *Acta Materialia* 61, no. 15 (2013): 5743-5755.
26. Tong, Chung-Jin, Min-Rui Chen, Jien-Wei Yeh, Su-Jien Lin, Swe-Kai Chen, Tao-Tsung Shun, and Shou-Yi Chang. "Mechanical performance of the  $Al_xCoCrCuFeNi$  high-entropy alloy system with multiprincipal elements." *Metallurgical and Materials Transactions A* 36, no. 5 (2005): 1263-1271.
27. Shun, Tao-Tsung, and Yu-Chin Du. "Microstructure and tensile behaviors of FCC  $Al_{0.3}CoCrFeNi$  high entropy alloy." *Journal of Alloys and Compounds* 479, no. 1 (2009): 157-160.
28. Tsai, Che-Wei, Yu-Liang Chen, Ming-Hung Tsai, Jien-Wei Yeh, Tao-Tsung Shun, and Swe-Kai Chen. "Deformation and annealing behaviors of high-entropy alloy  $Al_{0.5}CoCrCuFeNi$ ." *Journal of Alloys and Compounds* 486, no. 1 (2009): 427-435.
29. Koželj, Primož, S. Vrtnik, A. Jelen, S. Jazbec, Z. Jagličić, S. Maiti, M. Feuerbacher, W. Steurer, and J. Dolinšek. "Discovery of a superconducting high-entropy alloy." *Physical Review Letters* 113, no. 10 (2014): 107001.
30. Kao, Yih-Farn, Swe-Kai Chen, Ting-Jie Chen, Po-Chou Chu, Jien-Wei Yeh, and Su-Jien Lin. "Electrical, magnetic, and Hall properties of  $Al_xCoCrFeNi$  high-entropy alloys." *Journal of Alloys and Compounds* 509, no. 5 (2011): 1607-1614.
31. Singh, S., N. Wanderka, K. Kiefer, K. Siemensmeyer, and J. Banhart. "Effect of decomposition of the Cr-Fe-Co rich phase of  $AlCoCrCuFeNi$  high entropy alloy on magnetic properties." *Ultramicroscopy* 111, no. 6 (2011): 619-622.
32. Lucas, M.S., L. Mauger, J.A. Munoz, Yuming Xiao, A.O. Sheets, S.L. Semiatin, J. Horwath, and Z. Turgut. "Magnetic and vibrational properties of high-entropy alloys." *Journal of Applied Physics* 109, no. 7 (2011): 07E307.
33. Senkov O, Wilks G, Miracle D, Chuang C, Liaw P. Refractory high-entropy alloys. *Intermetallics* 2010; 18: 1758-1765
34. Senkov O, Wilks G, Scott J, Miracle D. Mechanical properties of Nb25Mo25Ta25W25 and V20Nb20Mo20Ta20W20 refractory high entropy alloys. *Intermetallics* 2011; 19: 698-706
35. Senkov O, Scott J, Senkova S, Miracle D, Woodward C. Microstructure and room temperature properties of a high-entropy TaNbHfZrTi alloy. *Journal of Alloys and Compounds* 2011; 509: 6043-6048.
36. Lu, Yiping, Yong Dong, Sheng Guo, Li Jiang, Huijun Kang, Tongmin Wang, Bin Wen et al. "A promising new class of high-temperature alloys: eutectic high-entropy alloys." *Scientific Reports* 4 (2014).

37. Lv, Z.Y., X.J. Liu, B. Jia, H. Wang, Y. Wu, and Z.P. Lu. "Development of a novel high-entropy alloy with eminent efficiency of degrading azo dye solutions." *Scientific Reports* 6 (2016).
38. Miracle, D.B., and O.N. Senkov. "A critical review of high entropy alloys and related concepts." *Acta Materialia* 122 (2017): 448-511.
39. Senkov, O.N., J.D. Miller, D.B. Miracle, and C. Woodward. "Accelerated exploration of multi-principal element alloys with solid solution phases." *Nature Communications* 6 (2015).
40. Troparevsky, M. Claudia, James R. Morris, Markus Daene, Yang Wang, Andrew R. Lupini, and G. Malcolm Stocks. "Beyond atomic sizes and Hume-Rothery rules: understanding and predicting high-entropy alloys." *JOM* 67, no. 10 (2015): 2350-2363.
41. Zhou, Y.J., Zhang, Y., Wang, Y.L. & Chen, G.L. Solid solution alloys of AlCoCrFeNiTix with excellent room-temperature mechanical properties. *Appl. Phys. Lett.* 90, 181904 (2007).
42. Yao, M.J., Pradeep, K.G., Tasan, C.C. & Raabe, D. A novel, single phase, non-equiautomic FeMnNiCoCr high-entropy alloy with exceptional phase stability and tensile ductility. *Scr. Mater.* 72–73, 5–8 (2014).
43. Sims, Chester Thomas, Norman S. Stoloff, and William C. Hagel. "Superalloys II." (1987).
44. Gwalani, B., D. Choudhuri, V. Soni, Y. Ren, M. Styles, J. Y. Hwang, S. J. Nam, H. Ryu, S. H. Hong, and R. Banerjee. "Cu assisted stabilization and nucleation of L1<sub>2</sub> precipitates in Al 0.3 CuFeCrNi 2 fcc-based high entropy alloy." *Acta Materialia* 129 (2017): 170-182.
45. Gwalani, B., V. Soni, D. Choudhuri, M. Lee, J.Y. Hwang, S.J. Nam, H. Ryu, S.H. Hong, and R. Banerjee. "Stability of ordered L1<sub>2</sub> and B<sub>2</sub> precipitates in face centered cubic based high entropy alloys-Al<sub>0.3</sub>CoFeCrNi and Al<sub>0.3</sub>CuFeCrNi<sub>2</sub>." *Scripta Materialia* 123 (2016): 130-134.
46. Tang, Q.H., Y. Huang, Y.Y. Huang, X.Z. Liao, T.G. Langdon, and P.Q. Dai. "Hardening of an Al<sub>0.3</sub>CoCrFeNi high entropy alloy via high-pressure torsion and thermal annealing." *Materials Letters* 151 (2015): 126-129.
47. Gwalani, B., Vishal Soni, Michael Lee, S.A. Mantri, Yang Ren, and R. Banerjee. "Optimizing the coupled effects of Hall-Petch and precipitation strengthening in a Al<sub>0.3</sub>CoCrFeNi high entropy alloy." *Materials & Design* 121 (2017): 254-260.
48. Shun, Tao-Tsung, Cheng-Hsin Hung, and Che-Fu Lee. "The effects of secondary elemental Mo or Ti addition in Al<sub>0.3</sub>CoCrFeNi high-entropy alloy on age hardening at 700°C." *Journal of Alloys and Compounds* 495, no. 1 (2010): 55-58.
49. Jiang, Li, Yiping Lu, Yong Dong, Tongmin Wang, Zhiqiang Cao, and Tingju Li. "Annealing effects on the microstructure and properties of bulk high-entropy CoCrFeNiTi 0.5 alloy casting ingot." *Intermetallics* 44 (2014): 37-43.
50. Gwalani, Bharat, Vishal Soni, Talukder Alam, and Raj Banerjee. "Designing and characterizing a complex concentrated gamma/gamma prime 'superalloy'." *Microscopy and Microanalysis* 22, no. S3 (2016): 672-673.
51. Shun, T.T., Chang, L.Y. & Shiu, M.H. Microstructure and mechanical properties of multiprincipal component CoCrFeNiMox alloys. *Materials Characterization* 70, 63–67 (2012).

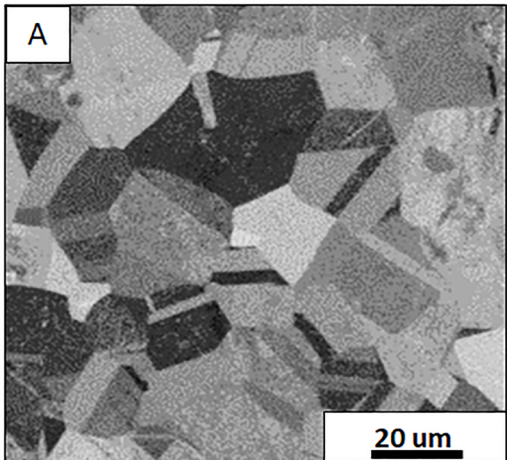
52. He, Feng, Zhijun Wang, Xuliang Shang, Chao Leng, Junjie Li, and Jincheng Wang. "Stability of lamellar structures in CoCrFeNiNb x eutectic high entropy alloys at elevated temperatures." *Materials & Design* 104 (2016): 259-264.
53. He, Feng, Zhijun Wang, Peng Cheng, Qiang Wang, Junjie Li, Yingying Dang, Jincheng Wang, and C.T. Liu. "Designing eutectic high entropy alloys of CoCrFeNiNb<sub>x</sub>." *Journal of Alloys and Compounds* 656 (2016): 284-289.
54. Liu, W.H., Z.P. Lu, J.Y. He, J.H. Luan, Z.J. Wang, B. Liu, Yong Liu, M.W. Chen, and C.T. Liu. "Ductile CoCrFeNiMox high entropy alloys strengthened by hard intermetallic phases." *Acta Materialia* 116 (2016): 332-342.
55. He, Feng, Zhijun Wang, Sizhe Niu, Qingfeng Wu, Junjie Li, Jincheng Wang, C.T. Liu, and Yingying Dang. "Strengthening the CoCrFeNiNb<sub>0.25</sub> high entropy alloy by FCC precipitate." *Journal of Alloys and Compounds* 667 (2016): 53-57.
56. Jiao, Zhi-Ming, Sheng-Guo Ma, Guo-Zheng Yuan, Zhi-Hua Wang, Hui-Jun Yang, and Jun-Wei Qiao. "Plastic Deformation of Al<sub>0.3</sub>CoCrFeNi and AlCoCrFeNi High-Entropy Alloys Under Nanoindentation." *Journal of Materials Engineering and Performance* 24, no. 8 (2015): 3077-3083.
57. Li, Z., S. Zhao, H. Diao, P.K. Liaw, and M.A. Meyers. "High-velocity deformation of Al<sub>0.3</sub>CoCrFeNi high-entropy alloy: Remarkable resistance to shear failure." *Scientific Reports* 7 (2017).
58. Ma, S.G., S.F. Zhang, M.C. Gao, P.K. Liaw, and Y. Zhang. "A successful synthesis of the CoCrFeNiAl<sub>0.3</sub> single-crystal, high-entropy alloy by Bridgman solidification." *JOM* 65, no. 12 (2013): 1751-1758.
59. G.S. Pawley, Unit-cell refinement from powder diffraction scans, *J. Appl. Crystallogr.* 14.6 (1981) 357-361.
60. Hou, Jinxiong, Min Zhang, Shengguo Ma, Peter K. Liaw, Yong Zhang, and Junwei Qiao. "Strengthening in Al<sub>0.25</sub>CoCrFeNi high-entropy alloys by cold rolling." *Materials Science and Engineering: A* 707 (2017): 593-601.
61. Cahn, Robert W. "Lattice parameter changes on disordering intermetallics." *Intermetallics* 7, no. 10 (1999): 1089-1094.
62. Gwalani, B., T. Alam, C. Miller, T. Rojhirunsakool, Y. S. Kim, S. S. Kim, M. J. Kaufman, Yang Ren, and Rajarshi Banerjee. "Experimental investigation of the ordering pathway in a Ni-33 at.% Cr alloy." *Acta Materialia* 115 (2016): 372-384.
63. Andersson J.O., Helander T., Höglund L., Shi P.F., and Sundman B., (2002). Thermo-Calc and DICTRA, Computational tools for materials science. *Calphad*, 26, 273-312.
64. Frenkel, Yakovich Ilich. "Kinetic theory of liquids." (1955).
65. K.C. Russell, Nucleation in solids: The induction and steady state effects, *Adv. Coll. Inter. Sci.* 13 (1980) 205-318.
66. Y. Mishin, Calculation of the  $\gamma/\gamma'$  interface free energy in the Ni-Al system by the capillary fluctuation method, *Modelling and Simulation in Materials Science and Engineering* 22(4) (2014) 045001.
67. A.J. Ardell, Interfacial Free Energies and Solute Diffusivities from Data on Ostwald Ripening. *Interface Science* 3 (1995) 119–125.

68. A.J. Ardell, A<sub>1</sub>-L<sub>12</sub> interfacial free energies from data on coarsening in five binary Ni alloys, informed by thermodynamic phase diagram assessments. *J. Mate. Sci.* 46 (2011) 4832–4849.
69. Hopkins R.H. and Kossowsky R. The crystallography of phase interfaces in the Ni-Cr alloy system, *Acta Metall.* 19 (1971) 203-211.
70. Chen J K, Farkas, D and Reynolds, WT. Atomistic simulation of an fcc/bcc interface in Ni-Cr alloys, *Acta Mater.* 45 (1997) 4415.
71. Song Lu, Hualei Zhang, Qing-Miao Hu, Marko P J Punkkinen, Börje Johansson and Levente Vitos, Magnetic effect on the interfacial energy of the Ni(111)/Cr(110) interface, *J. Phys.: Condens. Matter* 26 (2014) 355001.
72. Chen J.K., Chen, G. and Reynolds, WT. Interfacial structure and growth mechanisms of lath-shaped precipitates in Ni-45 wt Cr, *Phil. Mag. A* 78 (1998) 405-408.
73. Yang, Z and Johnson, RA. An EAM simulation of the alpha - gamma iron interface, *Modelling Simul. Mater. Sci. Eng.* 1 (1993) 707.
74. G.I. Toth, J.R. Morris, and L. Granasy, Ginzburg-Landau-Type Multiphase Field Model for Competing fcc and bcc Nucleation, *Phys. Rev. Lett.* 106, (2011) 045701.
75. A. Malik, J. Odqvist, L.H. Glund, S. Hertzman, and J. Agren, Phase-Field Modeling of Sigma-Phase Precipitation in 25Cr7Ni4Mo Duplex Stainless Steel, *Mater. Trans. A* 48 (2017) 4914-4928.
76. Reed, Roger C. The superalloys: fundamentals and applications. Cambridge university press, 2008.





A



20  $\mu\text{m}$

B

[011]*fcc*

$\bar{2}00$

$\bar{1}1\bar{1}$

0

11 $\bar{1}$

C

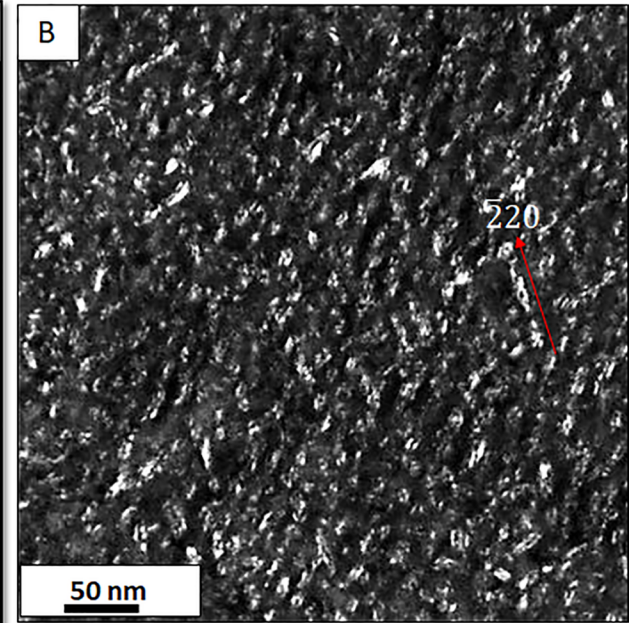
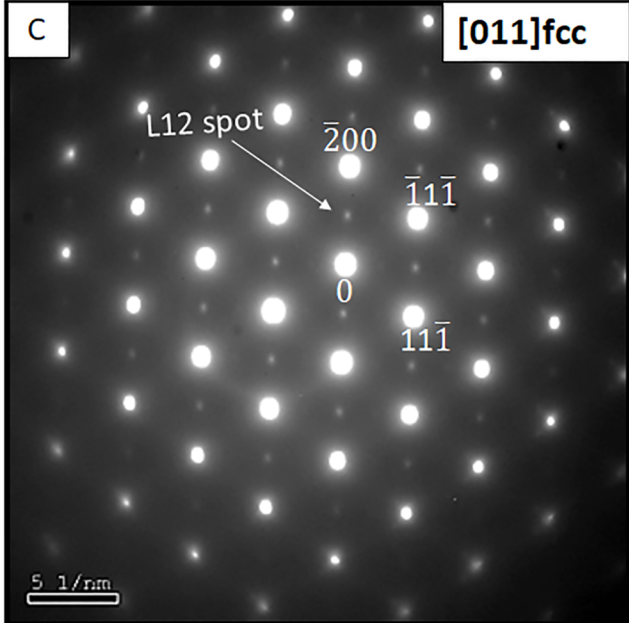
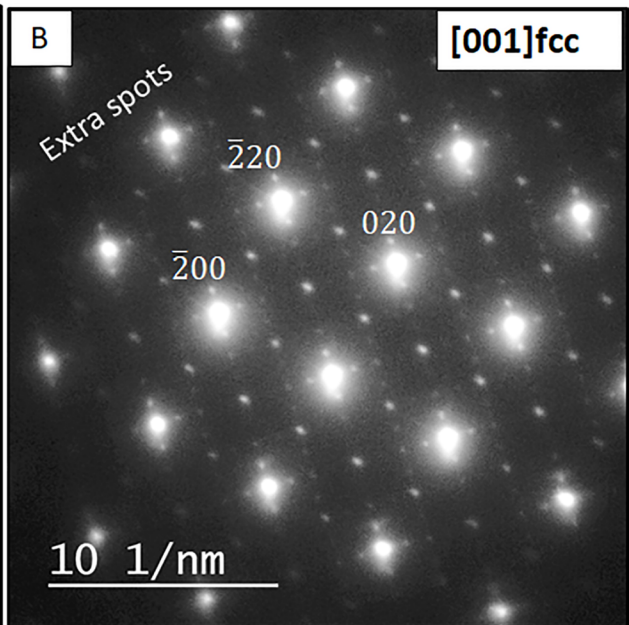
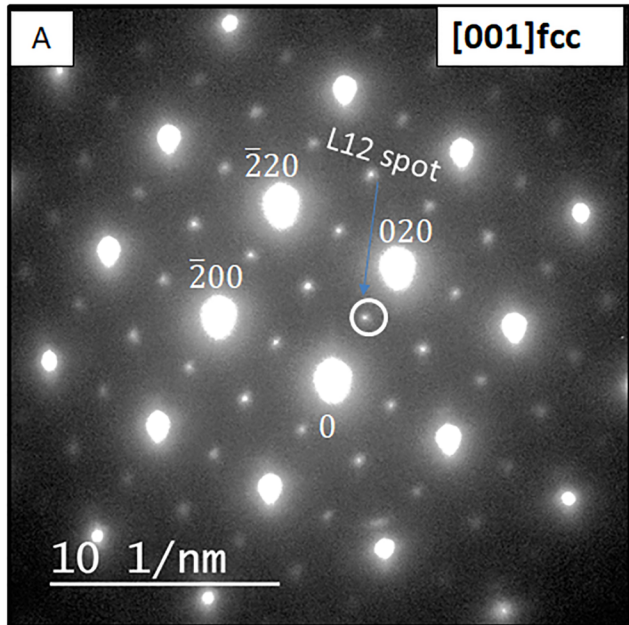
APT reconstruction

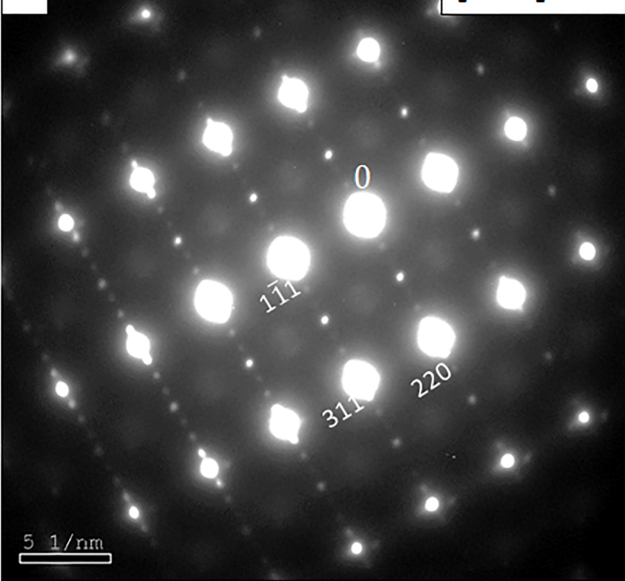
All ions

0.08  $\mu\text{m}$

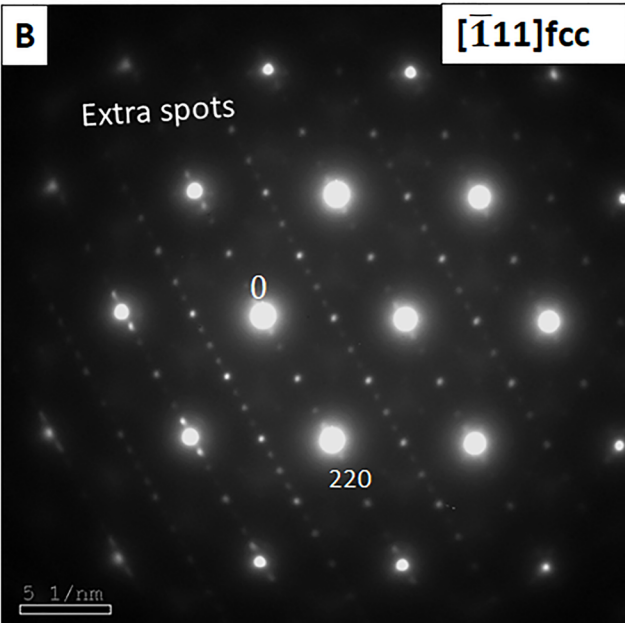
160 nm

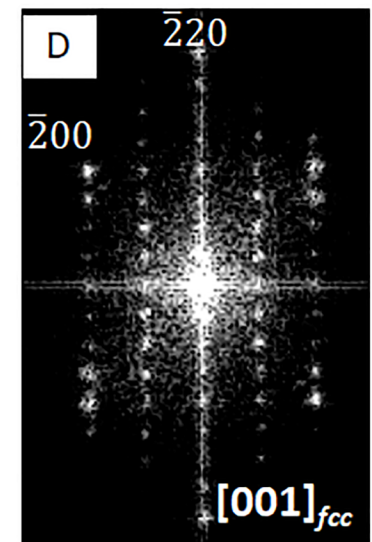
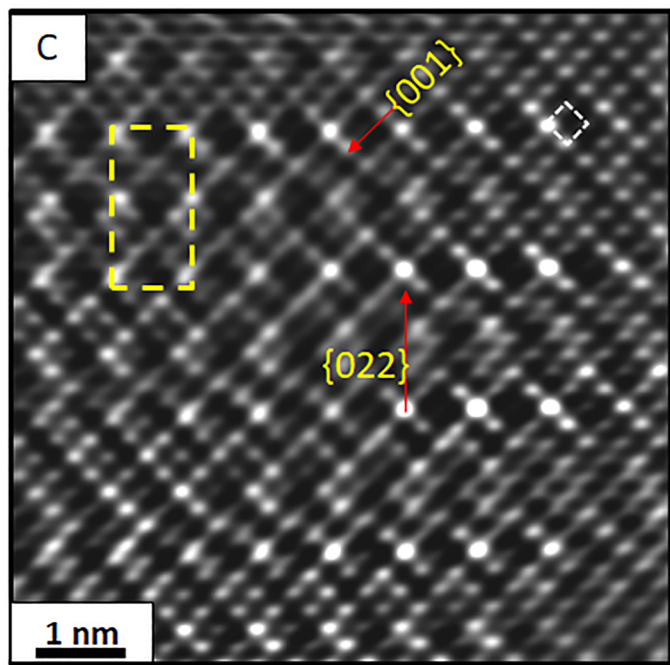
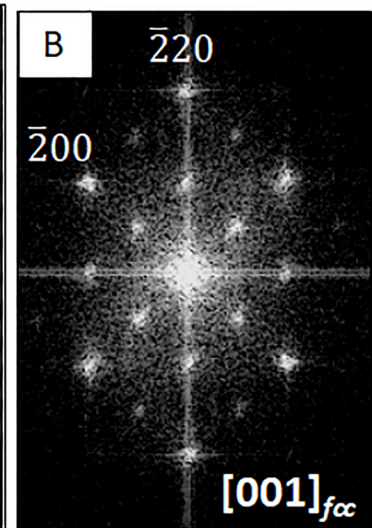
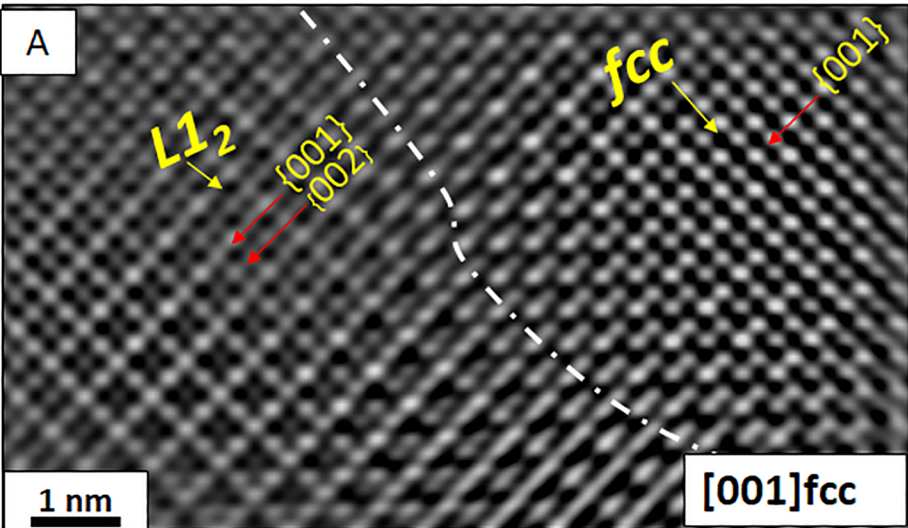
140 120 100 80 60 40 20 z

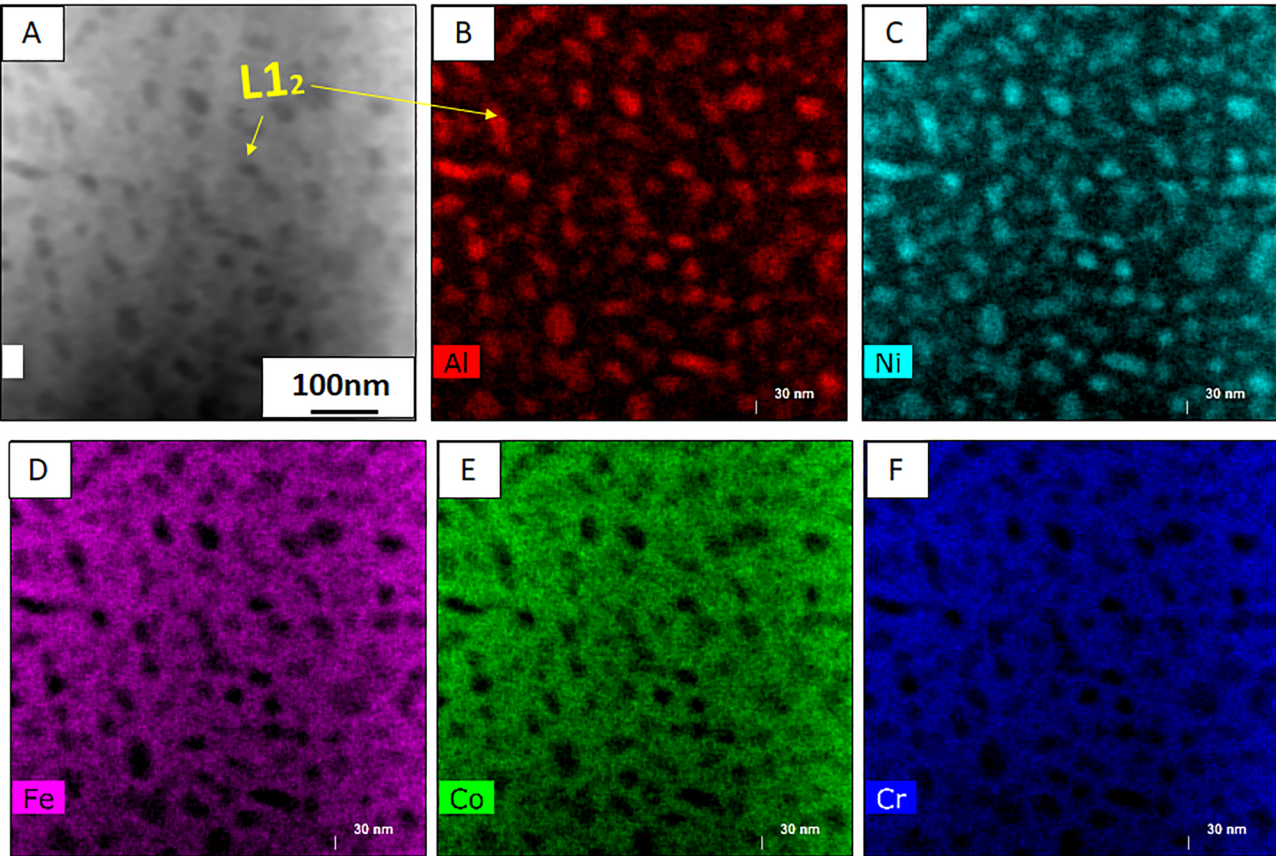


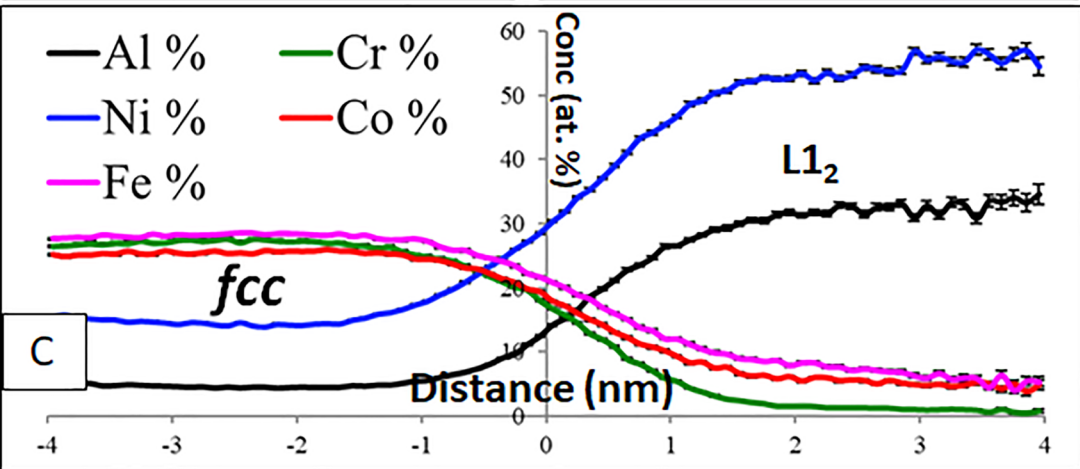
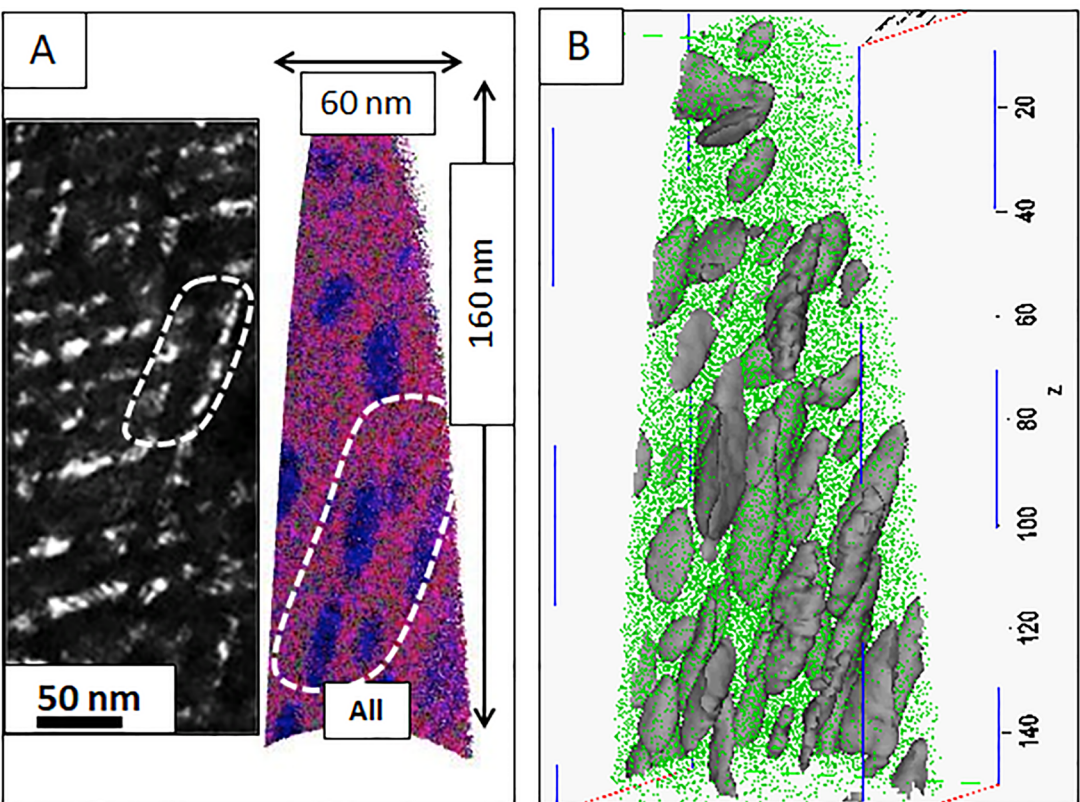
**A****[112]fcc****B****[111]fcc**

Extra spots

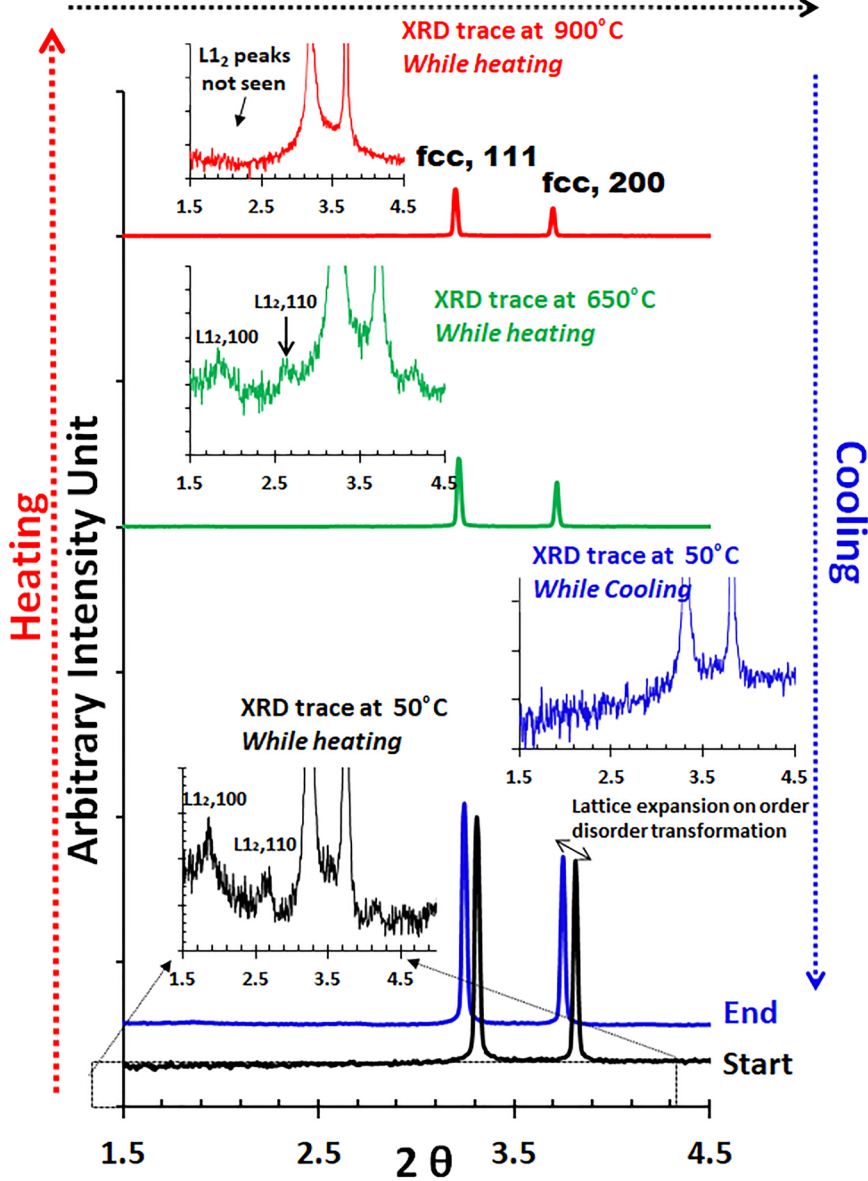




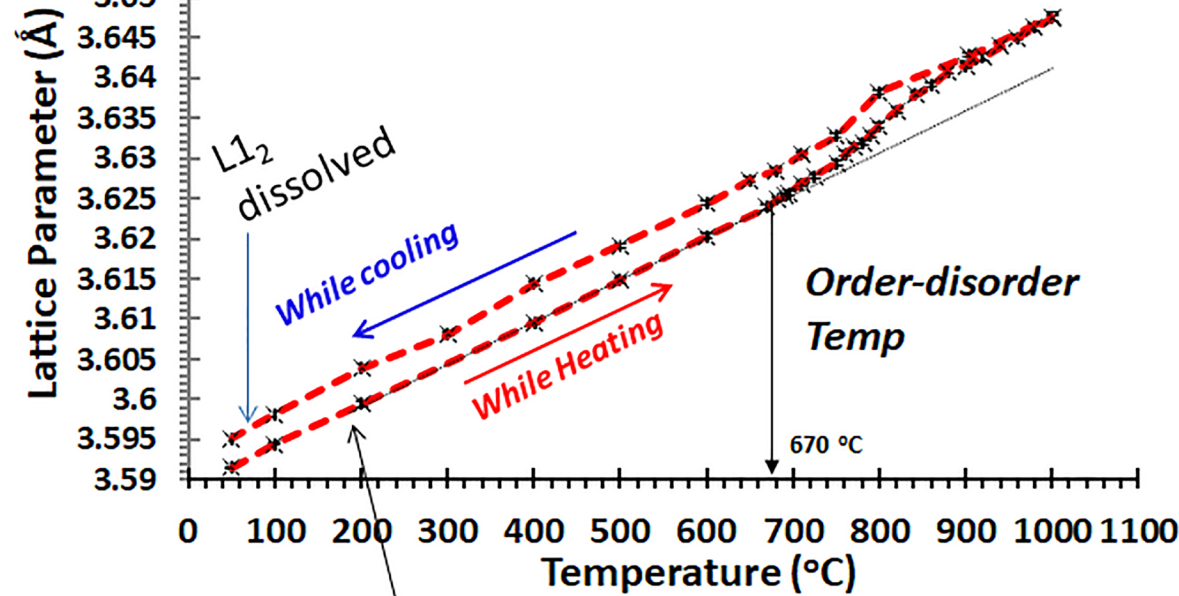




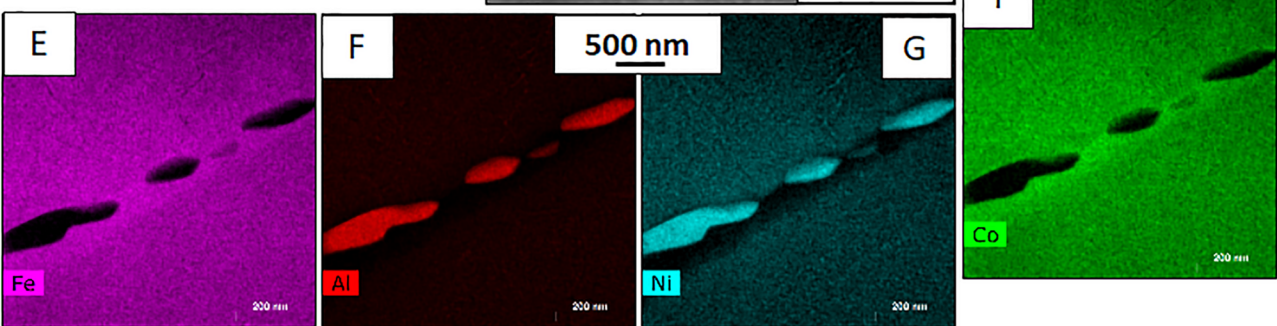
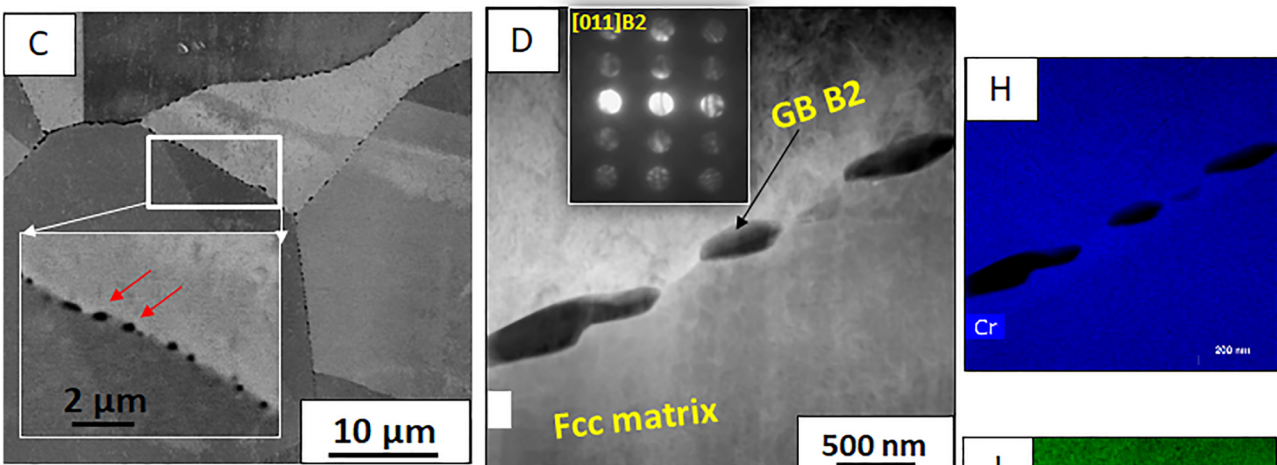
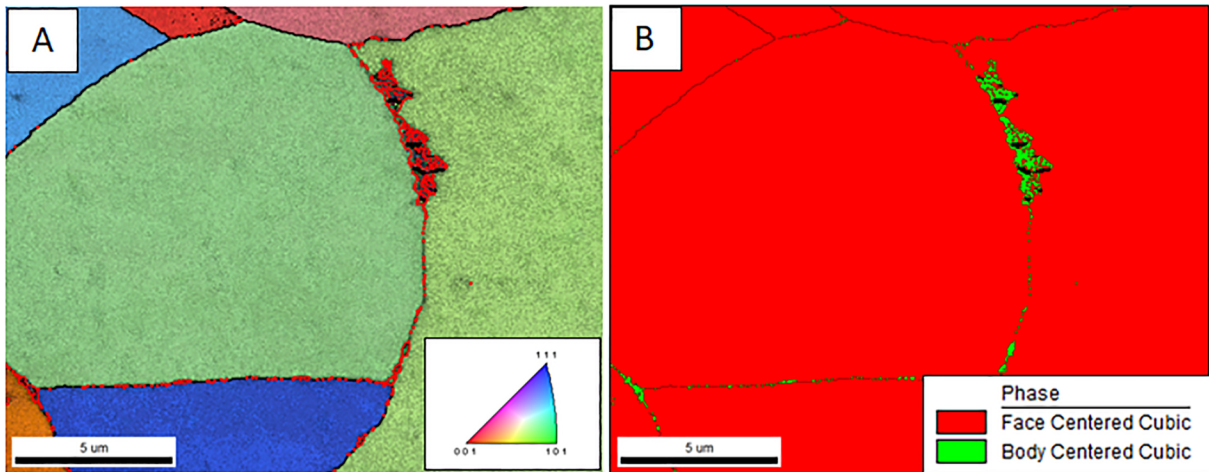
Heated to 1000 °C and cooled

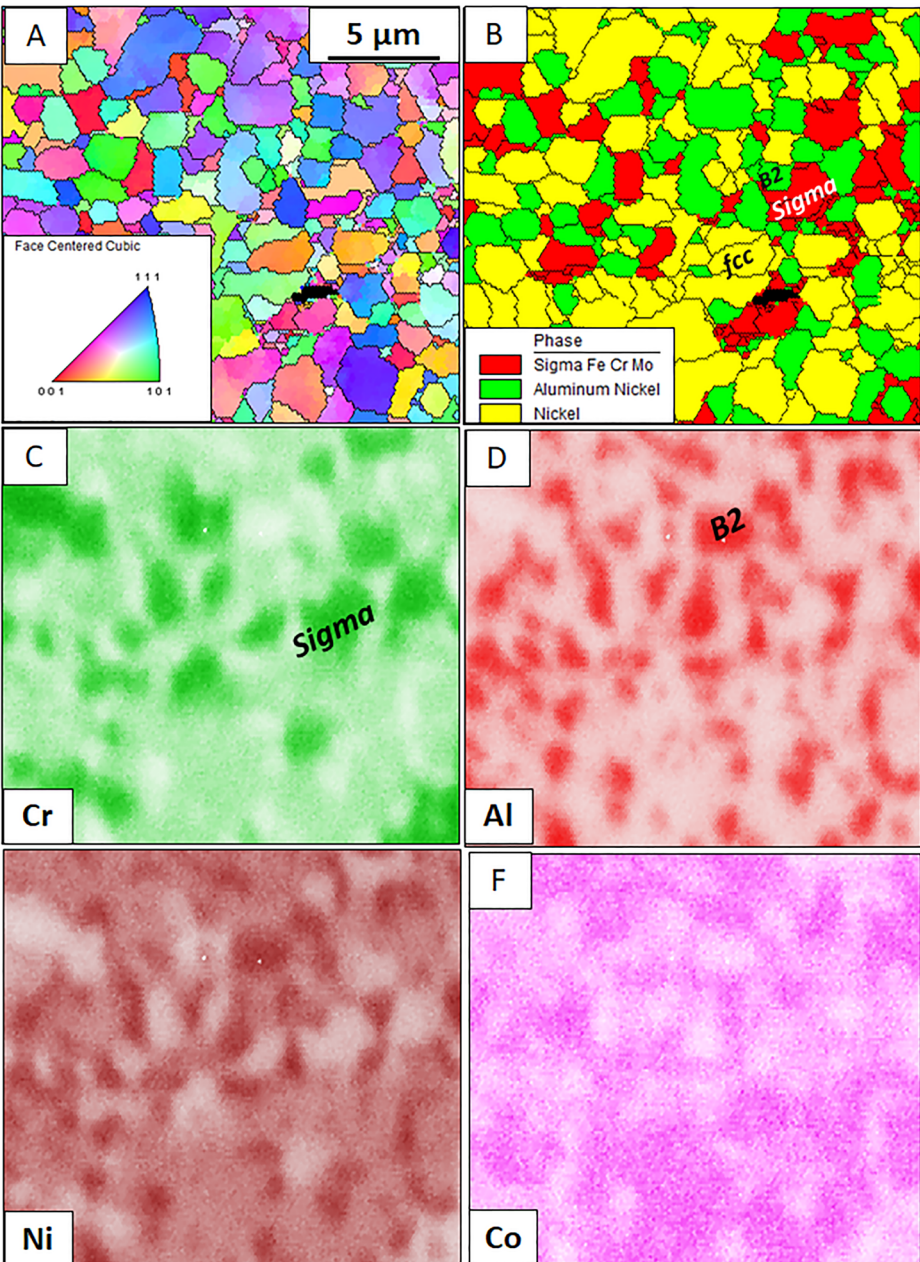


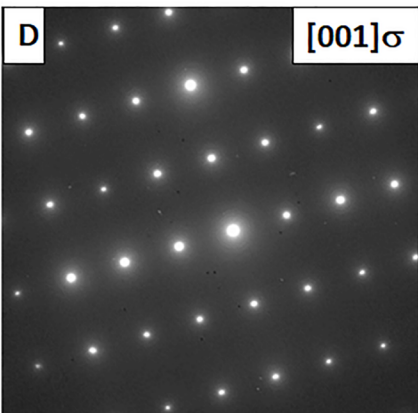
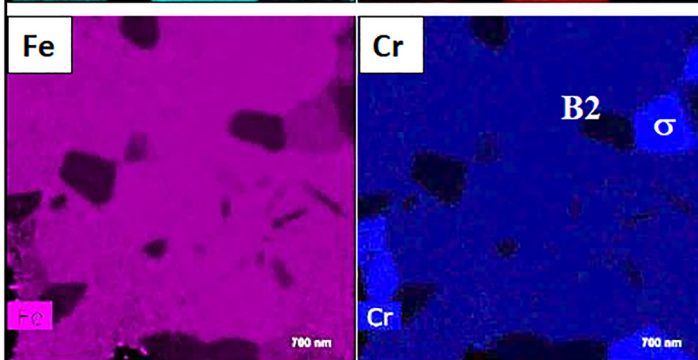
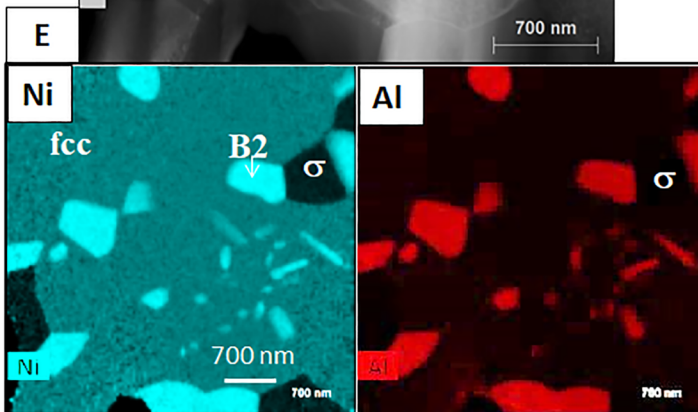
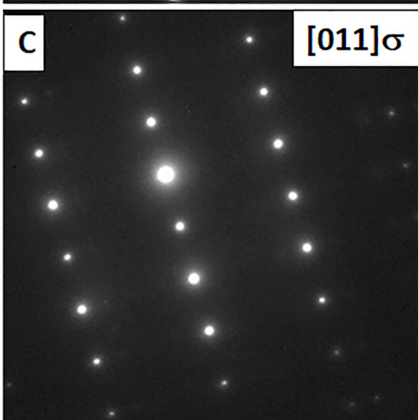
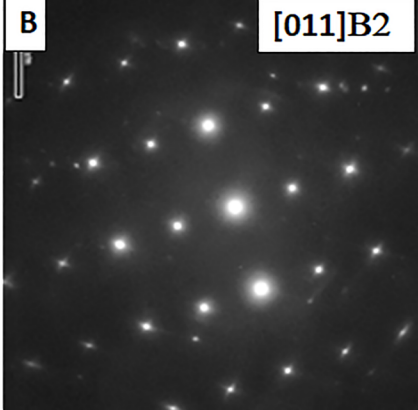
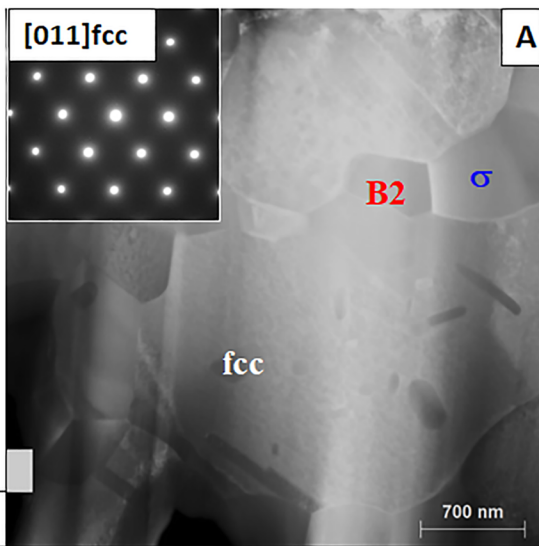
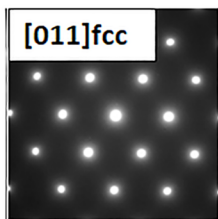
*CRSA-620 : fcc lattice parameter vs temperature*

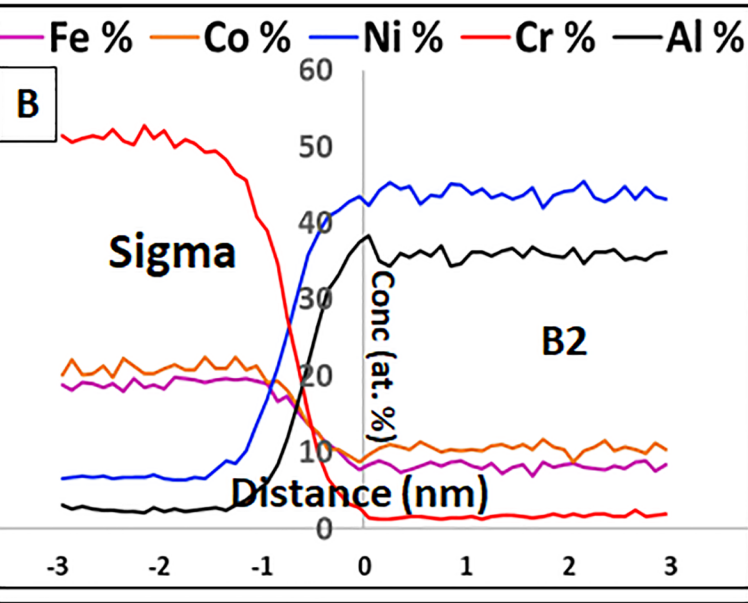
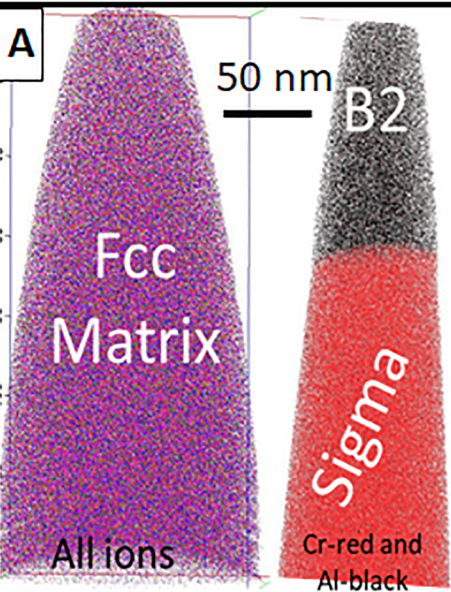


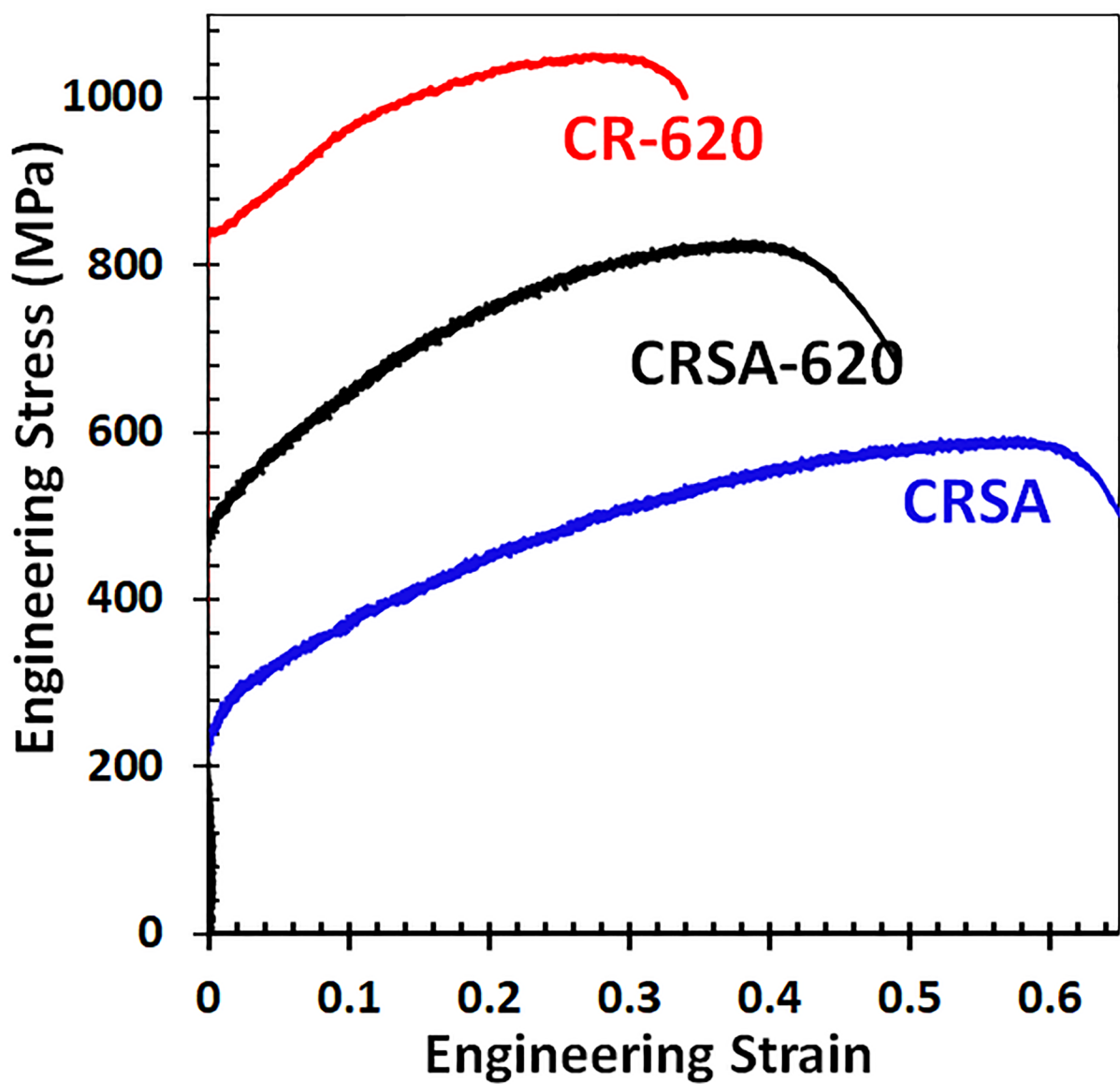
Starting microstructure consisted of *fcc + L1<sub>2</sub>* structure



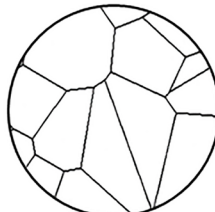




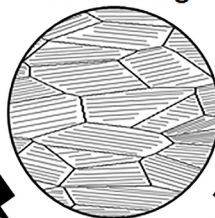
**A**



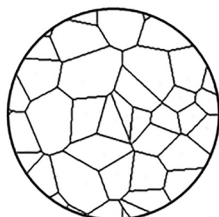
As-cast +  
homogenized



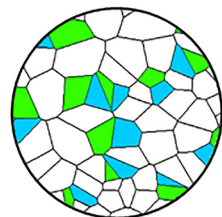
Cold rolling



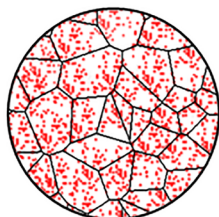
High temperature  
recrystallization



*fcc + B2 + σ*  
grains

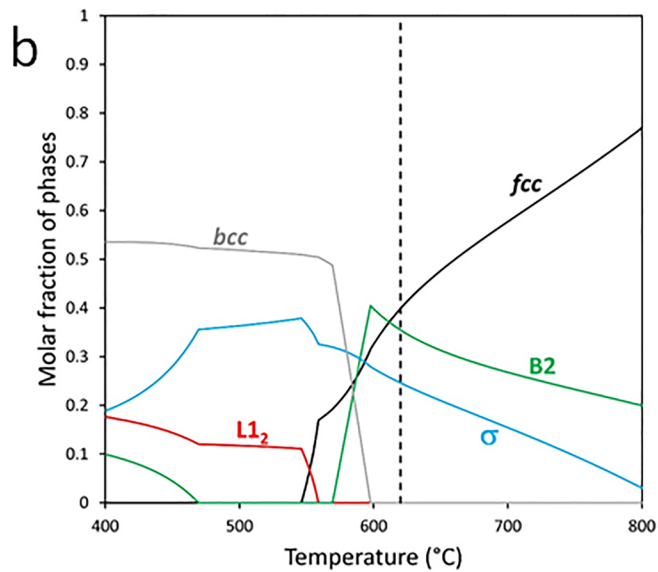
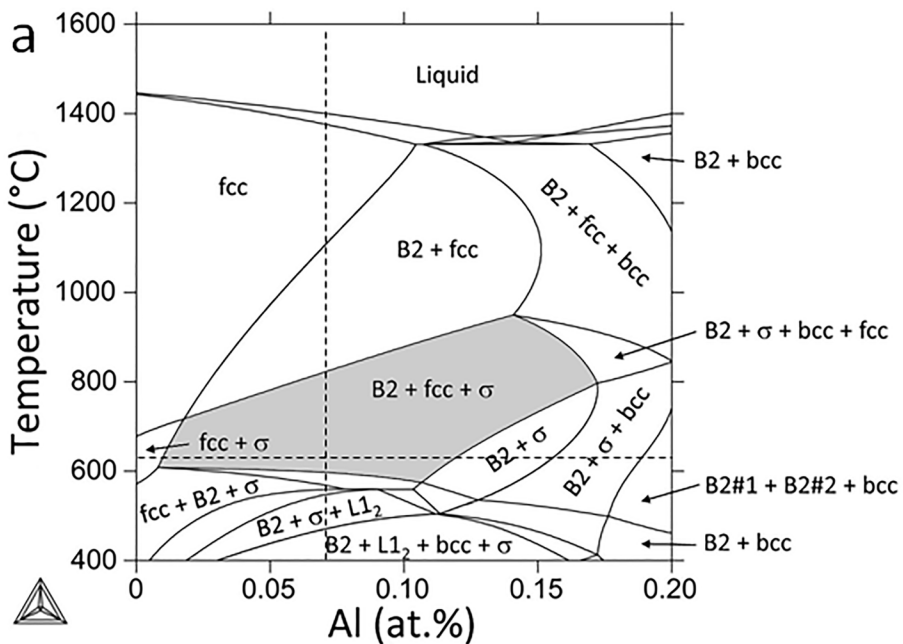


Precipitation annealing

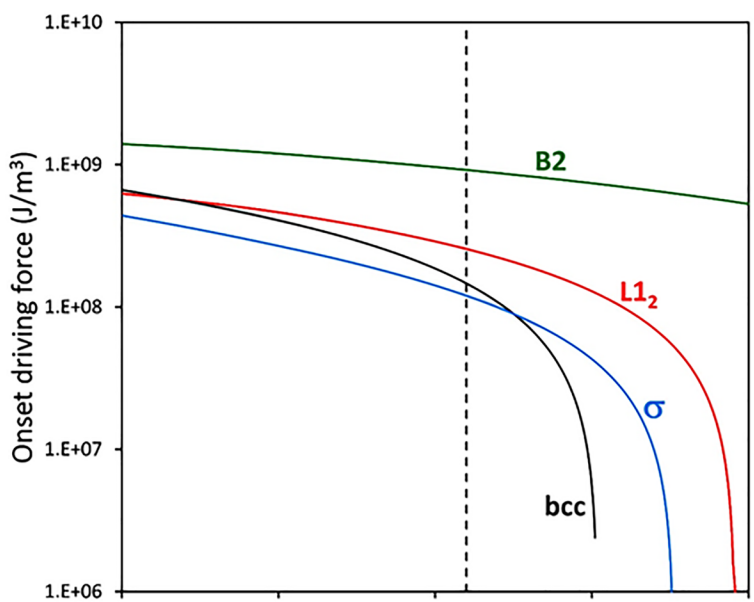


*fcc grains*  
+ p-L1<sub>2</sub>

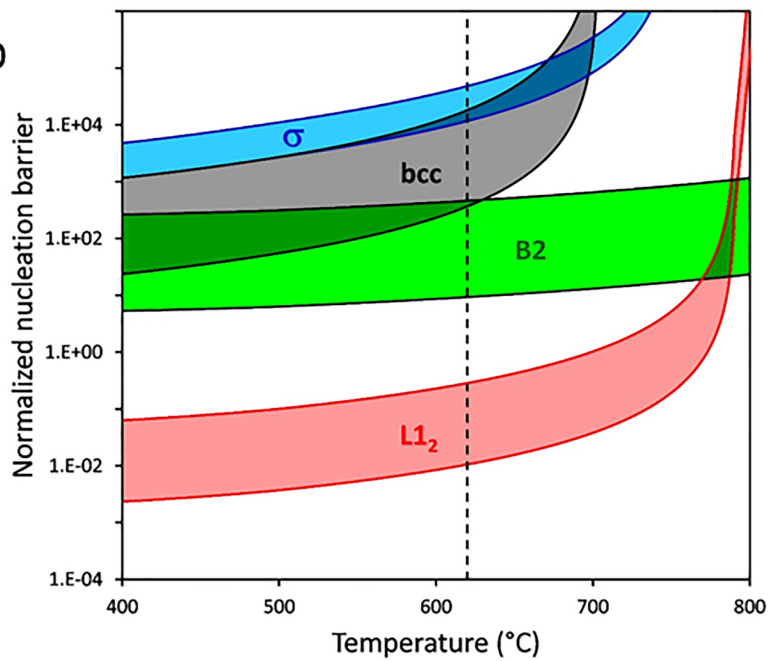
Precipitation  
strengthened



a

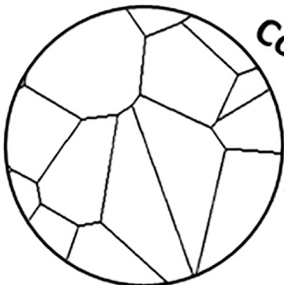


b

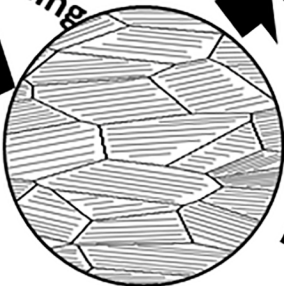


## *Modifying Transformation Pathways*

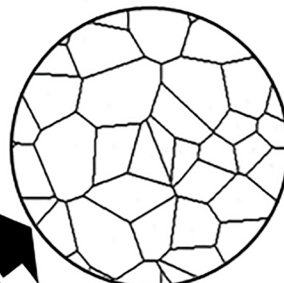
As-cast +  
homogenized



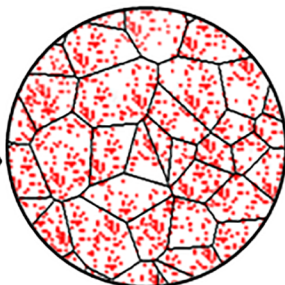
*Cold Rolling*



High temperature  
recrystallization

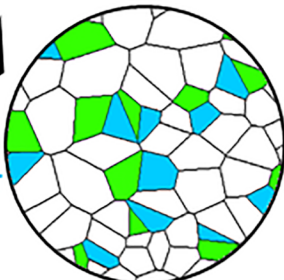


Precipitation  
annealing



*fcc grains*  
+ *p-L1<sub>2</sub>*

*fcc + B2 + σ*  
grains



Tri-phase